Preprint typeset using LaTeX style emulateapj v. 5/2/11

arXiv:1610.08610v1 [astro-ph.GA] 27 Oct 2016

THE PHYSICAL ENVIRONMENT AROUND IRAS 17599-2148: INFRARED DARK CLOUD AND BIPOLAR NEBULA

L. K. Dewangan[1], D. K. Ojha[2], I. Zinchenko[3], P. Janardhan[1], S. K. Ghosh[4], and A. Luna[5]

ABSTRACT

We present a multi-scale and multi-wavelength study to investigate the star formation process around IRAS 17599−2148 that is part of an elongated filamentary structure (EFS) (extension ∼21 pc) seen in the *Herschel* maps. Using the *Herschel* data analysis, at least six massive clumps (M_{clump} ∼777 – 7024 $M_\odot$) are found in the EFS with a range of temperature and column density of ∼16–39 K and ∼0.6–11 × 10^{22} cm^{-2} (A_V ∼7–117 mag), respectively. The EFS hosts cold gas regions (i.e. infrared dark cloud) without any radio detection and a bipolar nebula (BN) linked with the H II region IRAS 17599−2148, tracing two distinct environments inferred through the temperature distribution and ionized emission. Based on virial analysis and higher values of self-gravitating pressure, the clumps are found unstable against gravitational collapse. We find 474 young stellar objects (YSOs) in the selected region and ∼72% of these YSOs are found in the clusters distributed mainly toward the clumps in the EFS. These YSOs might have spontaneously formed due to processes not related to the expanding H II region. At the edges of BN, four additional clumps are also associated with YSOs clusters, which appear to be influenced by the expanding H II region. The most massive clump in the EFS contains two compact radio sources traced in the GMRT 1.28 GHz map and a massive protostar candidate, IRS 1 prior to an ultracompact H II phase. Using the VLT/NACO near-infrared images, IRS 1 is resolved with a jet-like feature within a 4200 AU scale.

Subject headings: dust, extinction – H II regions – ISM: clouds – ISM: individual objects (IRAS 17599-2148) – stars: formation – stars: pre-main sequence

1. INTRODUCTION

In recent years, *Spitzer* has revealed many massive star-forming (MSF) regions which contain the infrared dark clouds (IRDCs), mid-infrared (MIR) shells or bubbles, 6.7 GHz methanol maser emission (MME), H II regions, and young star clusters together. It is indeed obvious that such sites host numerous complex physical processes of star formation. These sites offer to explore the key processes that govern the birth and feedback of massive stars ($\gtrsim$ 8 $M_\odot$) (e.g., Zinnecker & Yorke 2007; Deharveng et al. 2010; Rathborne et al. 2011; Tackenberg et al. 2012; Tan et al. 2014; Beuther et al. 2015; Ragan et al. 2015; Dewangan et al. 2015a,b; Xu et al. 2016). Furthermore, such regions also allow to understand the formation and evolution of stellar clusters. In particular, the understanding of star formation processes demands a multi-scale and multi-wavelength approach. However, the study of close and large environments of such MSF regions is still lacking, which will help us to gain better insight into the ongoing physical processes.

IRAS 17599−2148, situated at a distance of 4.2 kpc (Kim & Koo 2001), has a bipolar appearance at wavelengths longer than 2 μm (Dewangan et al. 2012). The bipolar nebula was referred as two MIR bubbles (CN107 and CN109; Churchwell et al. 2007). An H II region associated with IRAS 17599−2148 (i.e. G8.14+0.23 H II region) is excited by a single star of radio spectral class O6 (Kim & Koo 2001). The 20 cm continuum peak (Dewangan et al. 2012) and a Class II 6.7 GHz MME (peak velocity ∼19.83 km s^{-1}; Szymczak et al. 2012) were reported toward the waist of the bipolar nebula (see Figure 2 in Dewangan et al. 2012). Using the multi-wavelength analysis of the G8.14+0.23 H II region, Dewangan et al. (2012) found noticeable star formation activities on the periphery of the bipolar nebula and suggested an interaction of the H II region with its surroundings. Simon et al. (2006) reported the IRDC candidates around IRAS 17599−2148 (e.g. G008.25+00.16 and G008.20+00.18), which were identified based on the absorption features against the Galactic background in the 8.3 μm image. The integrated NANTEN ^{12}CO intensity map (beam size ∼ 2.′6) of the cloud associated with IRAS 17599−2148 was previously reported by Takeuchi et al. (2010), which was referred as M008.2+0.2 (V_{lsr} ∼19 km s^{-1}; a velocity range ∼12–25 km s^{-1}) in their work (see Figure 14b in Takeuchi et al. 2010). Based on the ^{12}CO gas distribution, the IRDC candidates traced in the 8.3 μm image are found to be physically linked with the molecular cloud M008.2+0.2 (see Figure 15 in Takeuchi et al. 2010). However, an investigation of star formation activity in these IRDCs is not yet carried out. Shirley et al. (2013) reported the spectroscopic HCO^+ (3–2) line observations toward the 1.1 mm dust continuum sources in the IRAS 17599−2148 region and some of them are found toward the IRDCs and the bipolar nebula. These dust continuum sources are traced in a velocity range of 18 to 21 km s^{-1}, which are in agree-

lokeshd@prl.res.in
[1] Physical Research Laboratory, Navrangpura, Ahmedabad - 380 009, India.
[2] Department of Astronomy and Astrophysics, Tata Institute of Fundamental Research, Homi Bhabha Road, Mumbai 400 005, India.
[3] Institute of Applied Physics of the Russian Academy of Sciences, 46 Ulyanov st., Nizhny Novgorod 603950, Russia.
[4] National Centre for Radio Astrophysics, Ganeshkhind, Pune - 411 007, India
[5] Instituto Nacional de Astrofísica, Óptica y Electrónica, Luis Enrique Erro # 1, Tonantzintla, Puebla, México C.P. 72840.

ment with the velocity of ionized gas (i.e. 20.3 km s^{-1}; Kim & Koo 2001). The knowledge of velocities of ionized gas, MME, and molecular gas confirms the physical association of the IRDC, MME, and bipolar nebula with the H II region linked with IRAS 17599−2148. Previous studies convincingly suggested that all these sources (i.e. H II region, IRDC, MME, and bipolar nebula) appear to be located in the same complex. Despite the availability of numerous observational data-sets, the understanding of close (below 10000 AU) and large (more than 10 pc) environments around the IRAS 17599−2148 region is missing. The ongoing physical processes around IRAS 17599−2148 are not systematically examined. In order to understand the physical environment and star formation processes around IRAS 17599−2148, we use the multi-wavelength data covering from the near-infrared (NIR) to radio wavelengths, which include the ESO Very Large Telescope (VLT) archival adaptive-optics NIR images and the Giant Metre-wave Radio Telescope (GMRT) radio continuum high-resolution maps at 0.61 and 1.28 GHz. The ESO-VLT NIR images are employed to probe the inner circumstellar environment of the infrared counterpart(s) (IRc) of exciting source(s) of the H II region and the 6.7 GHz MME. Our analysis is also focused to infer the distribution of dust temperature, column density, extinction, ionized emission, kinematics of molecular gas, and young stellar objects (YSOs). All together, such analysis helps us to characterize in depth the small and large-scale environments around IRAS 17599−2148, which will allow to understand the birth and feedback processes of massive stars as well as the formation and evolution of stellar clusters.

In Section 2, we provide the details of the multi-wavelength datasets used in this paper. In Section 3, we characterize the physical environment of the region around IRAS 17599−2148. Furthermore, we identify the stellar populations around the IRAS 17599−2148 region and infer their clustering. In Section 4, we discuss the possible star formation scenario based on our findings. Finally, in Section 5, we provide a summary of conclusions.

2. DATA AND ANALYSIS

Mutli-scale and multi-wavelength data have been used to explore the physical environments around IRAS 17599−2148. In this paper, we selected a region of ∼20.′8 × 13.′2 (∼25.4 pc × 16.1 pc at a distance of 4.2 kpc), centered at $\alpha_{2000} = 18^h02^m54.5^s$, $\delta_{2000} = -21°46'33.''6$.

2.1. *New Observations*

2.1.1. *Radio Continuum Observations*

Radio continuum observations of IRAS 17599−2148 at 0.61 and 1.28 GHz bands were obtained using the GMRT on 2012 Dec 29 and 2012 Dec 23 (Proposal Code: 23_054; PI: L. K. Dewangan), respectively. The radio data reduction was performed using the AIPS software, following similar method as described in Mallick et al. (2012, 2013). The 0.61 and 1.28 GHz maps have rms noise of 0.34 and 0.38 mJy/beam, respectively. The synthesized beam sizes of the final 0.61 and 1.28 GHz maps are ∼5.″6 × 5.″2 and ∼ 2.″8 × 2.″4, respectively.

Note that a large amount of emission from the Galactic plane was expected during the observations, which influences the low frequency observations and increases the effective antennae temperature. Since, IRAS 17599−2148 is located in the Galactic plane, our GMRT 0.61 and 1.28 GHz maps are corrected for system temperature (see Omar et al. 2002; Mallick et al. 2012, 2013; Baug et al. 2015). The details about the adopted procedure of system temperature corrections are described in Mallick et al. (2012, 2013).

2.2. *Archival data*

2.3. *NIR images*

2.3.1. *Adaptive-optics NIR images*

The imaging observations of IRAS 17599−2148 were taken with 8.2m VLT with NAOS-CONICA (NACO) adaptive-optics system (Lenzen et al. 2003; Rousset et al. 2003) in H-band ($\lambda_c = 1.66\,\mu$m, $\Delta\lambda = 0.33\,\mu$m), K_s-band ($\lambda_c = 2.18\,\mu$m, $\Delta\lambda = 0.35\,\mu$m) and L′-band ($\lambda_c = 3.80\,\mu$m, $\Delta\lambda = 0.62\,\mu$m). We downloaded these data from the ESO-Science Archive Facility (ESO proposal ID: 089.C-0455(A); PI: João Alves). The single frame exposure time was 21 s in L′-band, and 24 s in H- and K_s-bands. We used five H frames, five K_s frames, and eleven L′ frames. In each band, the final NACO image was obtained through the standard analysis procedure such as sky subtraction, image registration, combining with median method, and astrometric calibration, using IRAF and STAR-LINK softwares. The astrometric calibration of the NACO images was done using the UKIRT NIR Galactic Plane Survey (GPS; Lawrence et al. 2007) K-band point sources. The VLT/NACO H, K_s, and L′ images have resolutions of 0.″2 (∼840 AU), 0.″2 (∼840 AU), and 0.″1 (∼420 AU), respectively.

2.3.2. *UKIDSS GPS NIR Data*

Deep NIR photometric *JHK* magnitudes of point sources have been retrieved from the UKIDSS GPS sixth archival data release (UKIDSSDR6plus). The UKIDSS observations (resolution ∼0.″8) were carried out using the UKIRT Wide Field Camera (WFCAM; Casali et al. 2007). The UKIDSS GPS photometric data were calibrated using the Two Micron All Sky Survey (2MASS; Skrutskie et al. 2006) data. We extracted only reliable NIR photometric data following the recommendations given in Lucas et al. (2008) and Dewangan et al. (2015b). To avoid saturation, the sources were obtained fainter than J = 12.1, H = 11.1, and K = 10.0 mag in our selected GPS catalog. Furthermore, the 2MASS photometric magnitudes were retrieved for bright sources that were saturated in the GPS catalog.

2.4. *Spitzer Data*

Photometric images and magnitudes of point sources have been obtained from the *Spitzer*-Galactic Legacy Infrared Mid-Plane Survey Extraordinaire (GLIMPSE; Benjamin et al. 2003) survey at 3.6–8.0 μm (resolution ∼2″). The photometric magnitudes were extracted from the GLIMPSE-I Spring '07 highly reliable catalog. Additionally, we also obtained photometry of point sources from Dewangan et al. (2012) near the bipolar nebula, which are not listed in the GLIMPSE catalog (see Dewangan et al. 2012). The MIPS Inner Galactic Plane Survey (MIPSGAL; Carey et al. 2005) 24 μm data have

been utilized in this paper. The MIPSGAL 24 μm photometry has also been obtained from Gutermuth & Heyer (2015). We also performed aperture photometry in the MIPSGAL 24 μm image to extract point sources, which are not listed in the MIPSGAL 24 μm catalog. The photometry was extracted using a $7''$ aperture radius and a sky annulus from $7''$ to $13''$ in IRAF (e.g. Dewangan et al. 2015b). The MIPS zero-magnitude flux density, including aperture correction, was adopted for the photometric calibration, as listed in the MIPS Instrument Handbook-Ver-3.

2.5. *Herschel, ATLASGAL, and SCUBA-2 Data*

Far-infrared (FIR) and sub-millimeter (sub-mm) data adopted in this work have been retrieved from the *Herschel* Space Observatory data archives. The processed level2_5 images at 70 μm, 160 μm, 250 μm, 350 μm, and 500 μm were obtained using the *Herschel* Interactive Processing Environment (HIPE, Ott 2010). The beam sizes of these images are $5\farcs8$, $12''$, $18''$, $25''$, and $37''$ (Poglitsch et al. 2010; Griffin et al. 2010), respectively.

The Submillimetre Common-User Bolometer Array 2 (SCUBA-2) continuum map at 850 μm (beam size $\sim14''$) was obtained from the James Clerk Maxwell Telescope (JCMT) science archive. In our selected region, we also obtained the positions of fourteen dust clumps at 870 μm (Contreras et al. 2013) from the APEX Telescope Large Area Survey of the Galaxy (ATLASGAL; beam size $\sim19\farcs2$; Schuller et al. 2009).

2.6. *CO (J=3−2) Line Data*

The JCMT HARP CO (3-2) processed data cube was downloaded and the spatial resolution of the data cube is $16''$. The CO observations were observed on 11 June 2009. The data have a typical rms sensitivity (1σ) of ≈ 0.3 K.

3. RESULTS

3.1. *Large-scale environment around IRAS 17599−2148*

The distribution of molecular gas, dense materials, and ionized emission enables us to infer physical environment present in and around the IRAS 17599−2148 region.

3.1.1. *Infrared and molecular emission*

On a larger scale, an IRDC and a bipolar nebula, associated with the bright extended emission, are visually observed in the MIPSGAL 24 μm image (see Figure 1a). In the MIPSGAL 24 μm image, the embedded stellar sources are also seen toward the IRDC. Fourteen ATLASGAL dust continuum sources at 870 μm are also marked in Figure 1a. The ATLASGAL sources are found toward the IRDC and the bipolar nebula, tracing cold and dense regions. It appears as a chain of dense clumps/cores in our selected target region (e.g., Tafalla & Hacar 2015). In Figure 1a, the 24 micron image is saturated near the IRAS position, where the radio continuum peak position was reported (Becker et al. 1994; Dewangan et al. 2012). Figure 1b shows a three-color composite image made using *Herschel* 160 μm in red, *Herschel* 70 μm in green, and GLIMPSE 8.0 μm in blue. The IRDC appears as bright emission regions at wavelengths longer than 24 μm. The bipolar nebula is also seen as the brightest extended emission in Figure 1b. Figure 2a shows the ATLASGAL and *Herschel* sub-mm images of the region, which trace the cold dust emission (see Section 3.2 for quantitative estimate). The bipolar nebula is traced in all the *Herschel* images. Interestingly, we infer an elongated filamentary morphology (extension $\sim$21 pc) in the ATLASGAL and *Herschel* sub-mm images, where several condensations are found. Furthermore, the IRDC and the G8.14+0.23 H II region (including the bipolar nebula) are part of the filamentary structure (see a dashed curve in Figure 2a), which is embedded in the cloud associated with IRAS 17599−2148 (i.e. M008.2+0.2; see Figures 14b and 15 in Takeuchi et al. 2010). The integrated NANTEN ^{12}CO intensity map (beam size $\sim 2\farcm6$) traces a continuous velocity structure in the direction of IRAS 17599−2148 (Takeuchi et al. 2010). It includes the eastern and western sides of the bubble as well as the bubble itself (i.e., entire elongated filamentary structure; see Figure 14b in Takeuchi et al. 2010). Hence, this previous molecular line data, even with coarse beam size, further confirms the existence of the elongated filamentary structure. In Figure 2a, the *Herschel* images trace the faint dust emission (or infrared bridges) between the ATLASGAL dust continuum sources, which are located within the elongated filamentary structure. Taken together, the sub-mm images and the previously published CO line data reveal the existence of a single elongated filamentary structure in the region probed in this paper.

In Figure 2b, we present the JCMT CO(J = 3–2) gas emission in the direction of the IRAS position. Note that we do not have JCMT molecular line observations for the entire field of view, which is probed in this paper. The JCMT CO data are available only toward the bipolar nebula. Considering the better resolution of the JCMT HARP CO(3-2) data compared to the previously published NANTEN ^{12}CO data, we are able to observe the bipolar morphology in the integrated JCMT CO intensity map (in a velocity range of 14–26 km s^{-1}). The kinematics of molecular gas are described in Section 3.3. In Figure 2b, the 850 μm continuum emission, which traces the densest materials, is also overlaid on the integrated CO map and are mostly distributed toward the waist of the bipolar nebula. The 850 μm continuum map (beam size $\sim14''$) reveals two peaks (i.e. dense clumps/cores) and one of them coincides with a Class II 6.7-GHz MME. The 6.7 GHz MME is a reliable tracer of massive young stellar objects (MYSOs) (e.g. Walsh et al. 1998; Minier et al. 2001; Urquhart et al. 2013).

3.1.2. *Radio continuum emission*

In order to trace the distribution of ionized emission, we present high-resolution GMRT radio continuum maps at 0.61 GHz (beam size $\sim5\farcs6 \times 5\farcs2$) and 1.28 GHz (beam size $\sim2\farcs8 \times 2\farcs4$) of the region around IRAS 17599−2148. Figure 3 shows the GMRT 0.61 (top panel) and 1.28 GHz (bottom panel) contours overlaid on the *Spitzer* 4.5 μm image. Note that the radio emission is not detected toward the IRDC (not shown here) and is found only toward the previously known G8.14+0.23 H II region. However, these new maps provide more insight into the radio peak, due to high-resolution map, compared to previously reported radio continuum map at 20 cm (beam $\sim6''$) (Dewangan et al. 2012). Both the GMRT maps show the similar morphology of the ionized

emission and their peak positions are offset from the 6.7-GHz MME. The extended morphology and a single peak at 0.61 GHz map are similar as previously seen at 20 cm map (Dewangan et al. 2012). In addition to the extended morphology, due to high-resolution observations, the 1.28 GHz map has resolved a single peak (as seen in the 0.61 GHz map) into two compact peaks (see Figure 3b) (i.e., cp1 ($\alpha_{2000} = 18^h03^m01^s.49$, $\delta_{2000} = -21°48'12''.23$; peak flux density = 22.52 mJy/beam; angular size =$28.78'' \times 13.95''$; deconvolved size = $28.66'' \times 13.71''$); cp2 ($\alpha_{2000} = 18^h03^m01^s.38$, $\delta_{2000} = -21°48'13''.82$; peak flux density = 22.63 mJy/beam; angular size =$14.25'' \times 9.93''$; deconvolved size = $14.02'' \times 9.57''$)). Using the 1.28 GHz map, we computed the integrated flux densities equal to 1355.50 mJy and 480.12 mJy for cp1 and cp2 peaks, respectively. These integrated flux densities are utilized to compute the number of Lyman continuum photons (N_{uv}). The equation of N_{uv} is given by (Matsakis et al. 1976):

$$N_{uv}(s^{-1}) = 7.5 \times 10^{46} \left(\frac{S_\nu}{Jy}\right) \left(\frac{D}{kpc}\right)^2 \left(\frac{T_e}{10^4 K}\right)^{-0.45} \times \left(\frac{\nu}{GHz}\right)^{0.1} \quad (1)$$

where S_ν is the measured total flux density in Jy, D is the distance in kpc, T_e is the electron temperature, and ν is the frequency in GHz. The analysis is done for a distance of 4.2 kpc and for the electron temperature of 10000 K. We find N_{uv} (or logN_{uv}) to be $\sim 1.86 \times 10^{48}$ s^{-1} (48.27) and $\sim 6.6 \times 10^{47}$ s^{-1} (47.82) for cp1 and cp2, respectively. These estimates correspond to a single ionizing star of spectral type O8V–O8.5V and O9V–O9.5V (see Table 1 in Martins et al. (2005) for theoretical values) for cp1 and cp2, respectively. Based on these results, within a $18''$ of the IRAS position, two radio O-spectral type sources and a 6.7 GHz MME (without radio peak) are present, indicating the presence of different early evolutionary stages of massive star formation. The search of the driving sources of the radio peaks and the 6.7 GHz MME is presented in Section 3.4.

We also computed the integrated flux densities of the extended radio morphology seen (at 3-σ) in both the radio maps. Using equation 1, the estimation of N_{uv} is also performed for both the radio frequencies (0.61 GHz and 1.28 GHz) separately. Taking into account, D = 4.2 kpc, T_e = 10000 K, and $S_{1.28}$ = 3.39 Jy, we find N_{uv} (or logN_{uv}) = 4.7×10^{48} s^{-1} (48.67). Similarly, we obtain N_{uv} (or logN_{uv}) = 6.9×10^{48} s^{-1} (48.84) for D, T_e, and $S_{0.61}$ = 5.39 Jy. The estimates of N_{uv} values at different frequencies correspond to a single ionizing star of O6V–O6.5V spectral type (Martins et al. 2005), which is consistent with the previously reported spectral type of the ionizing source of the G8.14+0.23 H II region (e.g. Kim & Koo 2001).

Within the elongated filamentary structure, the radio emission is detected toward the IRAS 17599−2148 position and is absent toward the IRDC, revealing different evolutionary stages of star formation.

3.2. *Herschel temperature and column density maps*

In recent years, the *Herschel* temperature and column density maps have been very useful tool for studying the distribution of column density, temperature, extinction, and clump mass in a given star-forming region. In this section, we also present these maps of the selected region around IRAS 17599−2148. We produced the temperature and column density maps of the region, in a manner similar to that described in Mallick et al. (2015) (also see Dewangan et al. 2015b). Here, we also give a brief step-by-step description of the procedures.

The *Herschel* temperature and column density maps are obtained from a pixel-by-pixel spectral energy distribution (SED) fit with a modified blackbody to the cold dust emission in the *Herschel* 160–500 μm wavelengths. The *Herschel* 70 μm data are not included in the analysis, because the 70 μm emission is dominated by UV-heated warm dust. The *Herschel* image at 160 μm is in the units of Jy pixel^{-1} and the images at 250–500 μm are calibrated in the surface brightness unit of MJy sr^{-1}. The plate scales of the 160, 250, 350, and 500 μm images are 6.4, 6, 10, and 14 arcsec/pixel, respectively. Before the SED fit, all images were convolved to the angular resolution of 500 μm image ($\sim 37''$) and were brought to the same flux unit (i.e. Jy pixel^{-1}). Furthermore, the images were regridded to the pixel size of 500 μm image ($\sim 14''$). These procedures were performed using the convolution kernels available in the HIPE software. Next, the sky background flux level was determined to be 0.393, 1.125, 2.528, and −0.186 Jy pixel^{-1} for the 500, 350, 250, and 160 μm images (size of the selected region $\sim 7\farcm7 \times 8\farcm2$; centered at: $\alpha_{J2000} = 18^h03^m41^s$, $\delta_{J2000} = -20°52'49.6''$), respectively. The featureless dark area away from the selected target region, to avoid diffuse emission associated with the target, was carefully selected for the background estimation.

In the final step, a modified blackbody was fitted to the observed fluxes on a pixel-by-pixel basis, in order to obtain the maps (see equations 8 and 9 given in Mallick et al. 2015). The fitting was performed using the four data points for each pixel, retaining the dust temperature (T_d) and the column density ($N(H_2)$) as free parameters. In the calculations, we utilized a mean molecular weight per hydrogen molecule (μ_{H2}=) 2.8 (Kauffmann et al. 2008) and an absorption coefficient (κ_ν =) 0.1 (ν/1000 GHz)$^\beta$ cm^2 g^{-1}, including a gas-to-dust ratio (R_t =) of 100, with a dust spectral index of $\beta = 2$ (see Hildebrand 1983). The final temperature and column density maps (resolution $\sim 37''$) are shown in Figure 4.

The *Herschel* temperature map traces the IRDC in a temperature range of about 16–22 K, while the considerably warmer gas (T_d ~25-39 K) is found toward the IRAS position (including the H II region and the bipolar nebula; see Figure 4a). It implies that the cold gas is exclusively found toward the IRDC, while the warmer gas is detected toward the H II region. In Figure 4b, the IRDC and the bipolar nebula are traced with higher column densities. Several condensations are seen in the column density map (see Figure 4b). The condensation having the highest column density (peak $N(H_2)$ $\sim 1.1 \times 10^{23}$ cm^{-2}; A_V ~117 mag) is associated with the H II region and the 6.7 GHz MME. The relation between optical extinction and hydrogen column density ($A_V = 1.07 \times 10^{-21}\ N(H_2)$; Bohlin et al. 1978) is adopted here.

3.2.1. *Herschel clumps*

In the column density map, the *clumpfind* algorithm (Williams et al. 1994) has been applied to identify the clumps and their total column densities. Twelve clumps are identified, which are labeled in Figure 4b and their boundaries are also shown in Figure 4c. We estimated the masses of these clumps using their total column densities. The mass of a single clump can be computed using the formula:

$$M_{clump} = \mu_{H_2} m_H Area_{pix} \Sigma N(H_2) \quad (2)$$

where μ_{H_2} is assumed to be 2.8, $Area_{pix}$ is the area subtended by one pixel, and $\Sigma N(\mathrm{H_2})$ is the total column density. The mass of each *Herschel* clump is listed in Table 1. The table also contains an effective radius of each clump, which is provided by the *clumpfind* algorithm. The clump masses vary between 410 $\mathrm{M_\odot}$ and 7024 $\mathrm{M_\odot}$. The elongated filamentary structure is associated with at least six massive clumps (i.e. IDs 1–5 and 10), indicating the fragmentation of the cloud. The most massive condensation (i.e ID 1) hosts two compact radio continuum sources and the 6.7 GHz MME, which is located at the waist of the bipolar nebula. At least three massive and cold condensations (i.e. IDs 3–5) are seen toward the IRDC. At least four condensations (i.e. IDs 6–8 and 12) are also found at the edges of the bipolar nebula.

In order to examine the internal dynamical properties of these clumps in more detail, we computed their physical parameters (such as, spherical free-fall time, virial mass, virial parameter, self-gravitating pressure, and Mach number). Using mass (M_{clump}) and radius (R_c) of each clump, we can estimate the mean mass density ρ_0, and the spherical free-fall time, $(t_{ff,sph})$ $= (3\pi/32G\rho_0)^{1/2}$ $(= 16.6(R_c/pc)^{3/2}(M_{clump}/M_\odot)^{-1/2}$ Myr). We estimated $t_{ff,sph}$ values for our identified clumps range from 0.4 to 0.77 Myr, which are tabulated in Table 1.

In each clump, the pressure exerted by the self-gravity of the molecular gas can be estimated using $P_{clump} \approx \pi G(M_{clump}/\pi R_c^2)^2$. The value of P_{clump} is tabulated in Table 1. In general, the pressure associated with a typical cool molecular cloud (P_{MC}) is found to be $\sim 10^{-11}$–10^{-12} dynes $\mathrm{cm^{-2}}$ (for a temperature $\sim$20 K and the particle density $\sim 10^3$–10^4 $\mathrm{cm^{-3}}$) (see Table 7.3 of Dyson & Williams 1980), which is much lower than P_{clump}. This comparison indicates an acting of self-gravity and a signature of star formation activity in these clumps.

To infer whether the identified clumps are stable and unstable against gravitational collapse, the virial mass analysis is employed. As mentioned above, we find six clumps associated with the filamentary structure and two of them are located at the waist of the bipolar nebula. The molecular line observations were reported toward four out of these six clumps. We estimated virial mass (M_{vir}) and virial parameter ($\mathrm{M}_{vir}/M_{clump}$) for these four clumps where line-width values were measured. The virial mass of a clump of radius R_c (in pc) and line-width ΔV (in km $\mathrm{s^{-1}}$) is defined as M_{vir} $(M_\odot) = \mathrm{k\,R}_c\,\Delta V^2$ (MacLaren et al. 1988), where the geometrical parameter, $\mathrm{k} = 126$, for a density profile $\rho \propto 1/\mathrm{r}^2$. A virial parameter less than 1 suggests a clump prone to collapse, and greater than 1 is resistant to collapse. For these clumps, the virial parameter is less than 1, indicating unstable clumps against gravitational collapse.

Following Dewangan et al. (2016), we estimated thermal sound speed (a_s) and non-thermal velocity dispersion (σ_{NT}) of the two clumps where gas kinetic temperature (T_{kin}) values were reported (Wienen et al. 2012). Wienen et al. (2012) estimated T_{kin} for clumps 1 and 2 to be 22.86 and 17.71 K, respectively. The sound speed a_s $(= (kT_{kin}/\mu m_H)^{1/2})$ is computed using T_{kin} and μ=2.37 (approximately 70% H and 28% He by mass). The non-thermal velocity dispersion is defined by:

$$\sigma_{\mathrm{NT}} = \sqrt{\frac{\Delta V^2}{8\ln 2} - \frac{kT_{kin}}{17 m_H}} = \sqrt{\frac{\Delta V^2}{8\ln 2} - \sigma_{\mathrm{T}}^2}, \quad (3)$$

where ΔV is the measured line-width of the observed $\mathrm{NH_3}$ spectra, σ_{T} $(= (kT_{kin}/17m_H)^{1/2})$ is the thermal broadening for $\mathrm{NH_3}$ at T_{kin} (e.g. Dunham et al. 2011), and m_H is the mass of the hydrogen atom. We obtain a_s and σ_{NT} to be 0.28 and 1.42 for clump 1, respectively, while $a_s = 0.25$ and $\sigma_{NT} = 1.44$ for clump 2, respectively. These values give us the Mach Numbers (σ_{NT}/a_s) to be 5 and 5.8 for clumps 1 and 2, respectively, indicating that these clumps are supersonic where non-thermal motions are dominated. The non-thermal motions could be explained by turbulence and outflows from YSOs.

3.3. *Velocity field*

Previously, Dewangan et al. (2012) studied the G8.14+0.23 H II region and suggested the possibility of triggered star formation by the expansion of this H II region. In order to further examine the expansion of the H II region, we present a kinematic analysis of the molecular gas in the G8.14+0.23 H II region. In Figure 5, the integrated CO intensity map and the position-velocity diagrams are presented. The position-velocity diagrams of the CO emission are shown with different position angles, tracing an C-like and a ring-like structure. Recently, Arce et al. (2011) studied the molecular gas distribution in the Perseus molecular cloud and compared a model of expanding bubbles in a turbulent medium. These authors predicted a C-like or ring-like structure for an expanding shell/bubble in the position-velocity diagrams (see Figure 5 in Arce et al. (2011)). In this work, the radio continuum maps suggest that the H II region associated with IRAS 17599−2148 can be excited by a single source of radio spectral O6V–O6.5V. Hence, the structures seen in the position-velocity diagrams can be explained by the expanding H II region with an expansion velocity of the gas to be $\sim$4.5 km $\mathrm{s^{-1}}$.

Furthermore, the position-velocity diagrams show a noticeable velocity gradient toward the IRAS 17599−2148 region, indicating the presence of a molecular outflow(s). Due to coarse beam of CO (3-2) line data, it is indeed difficult task to explore the real driver(s) of the outflow(s). Figure 6a shows the distribution of ionized and dust continuum emissions. It seems that the exciting source of the outflow could be driving source of the H II region or of the 6.7 GHz MME. Hence, high-resolution molecular line observations will be required to further explore the outflow activity in the IRAS 17599−2148 region.

Due to lack of the JCMT molecular line observations toward the IRDC, the analysis presented in this work does not provide any information of the molecular gas kinematics toward the IRDC.

3.4. *Small-scale environment toward IRAS 17599−2148*

In order to explore the driving source(s) of the 6.7 GHz MME and the radio continuum peaks, we examined the UKIDSS-GPS and GLIMPSE images toward IRAS 17599−2148 position. We also utilized the ESO-VLT NIR images to probe the inner circumstellar environment of the driving sources.

3.4.1. *Infrared counterpart of 6.7 GHz MME*

Figure 6b shows a three-color composite image made using the GLIMPSE images (5.8 μm in red; 4.5 μm in green; 3.6 μm in blue), which is also overlaid with the 1.28 GHz and 850 μm emission. A point-like source appears the reddest and brightest in the *Spitzer* images, and is located very close to the sub-mm emission peak (a projected linear separation of $\sim$8$''$) and the 6.7-GHz MME (a projected linear separation of $\sim$4$''$). The source was previously designated as IRS 1 and was characterized as a candidate MYSO (stellar mass $\sim$10$\pm$2 M$_{\odot}$) based on its SED modeling from the NIR to sub-mm data (see Figure 11 in Dewangan et al. 2012). IRS 1 is barely observed in the GPS H-band image (not shown here), however, it is seen as a single object in the GPS K-band image (resolution $\sim$0.8$''$; not shown here) and the GLIMPSE 3.6–8.0 μm images (resolution $\sim$2$''$) (see Figure 6b). IRS 1 is an embedded source located very close to the peak of the 6.7 GHz MME and is associated with a clump having the highest column density. Additionally, considering IRS 1 as a single bright source in the GLIMSE images, we consider the IRS 1 source as an infrared counterpart (IRc) of the 6.7-GHz MME. At the sensitivity of the observed GMRT radio map (3σ $\sim$1.14 mJy beam^{-1}), IRS 1 is situated at a projected linear separation of $\sim$10$''$ from the radio peaks seen in the 1.28 GHz map, which suggests that IRS 1 is not associated with any radio continuum peak (or an ultracompact (UC) H II region; see Figure 6b). Hence, IRS 1 cannot be the powering source of the H II region associated with the IRAS 17599−2148 region. As mentioned before, the 6.7-GHz MME is a reliable tracer of MYSO (e.g. Walsh et al. 1998; Minier et al. 2001; Urquhart et al. 2013). All together, IRS 1 could be a genuine massive protostar candidate (mass $\sim$10$\pm$2 M$_{\odot}$) in a very early evolutionary stage, before the onset of an UCH II region. Based on the presence of two compact radio continuum sources (with the radio spectral class of O-type stars) and the MME, IRAS 17599−2148 region appears to be a very similar system like W42 (see Figure 2 in Dewangan et al. 2015b).

In order to study the small scale environment of IRS 1, we present the ESO-VLT archival NIR images. In Figure 7, we show the VLT/NACO adaptive-optics images of IRS 1 in H, K$_s$, and L$'$ bands. The VLT/NACO H-band image detects a faint point-like source, while K$_s$ and L$'$ images resolve the IRS 1 into at least three point-like sources (i.e. designated as IRS 1a, IRS 1b, and IRS 1c; see Figure 7b) within a scale of $\sim$4200 AU and one of the sources (i.e. IRS 1a) is associated with the diffuse emission (see Figures 7b and 7c). We find these sources in the separation range from $\sim$0.$''$33 (1390 AU) to $\sim$0.$''$57 (2400 AU). de Villiers et al. (2015) summarized that the 6.7 GHz masers switch on after the onset of the outflow. The diffuse emission seen below $\sim$4200 AU scale with IRS 1a might be linked with the outflow. In general, the NIR emission is attributed to scattered light escaping through the outflow cavity (e.g. Zhang & Tan 2011). Hence, the diffuse emission feature could be a jet, which appears as a narrow emission feature and may be located inside an outflow cavity as traced in the L$'$ image. Additionally, Urquhart et al. (2013) suggested the exclusive association of Class II 6.7 GHz methanol masers with MYSOs. Hence, IRS 1a could be the main massive protostar among other point-like sources in the IRS 1 system.

Additionally, the multiplicity of point-like sources has been observed around IRS 1 within a scale of 4200 AU. Massive stars are generally found in binary and multiple systems (Duchêne & Kraus 2013). For example, in M8 and W42 star-forming regions, the well characterized "O" stars are resolved into multiple sources using the high-resolution NIR images (Goto et al. 2006; Dewangan et al. 2015b). Around IRS 1, the multiple sources are found in the separation range from $\sim$0.$''$33 (1390 AU) to $\sim$0.$''$57 (2400 AU). Due to the coarse beam of the JCMT-SCUBA-2, the 850 μm map is unable to resolve the dense core associated with IRS 1 source. Based on the separation of the sources in IRS 1 multiple system, there is possibility of the core fragmentation that may explain the origin of multiple systems (see Tobin et al. 2016, and references therein).

Based on these indicative results, further detailed studies of IRS 1 are encouraged using high-resolution interferometric observations at longer wavelength.

3.4.2. *Infrared counterparts of compact radio peaks*

To trace the IRcs of two compact radio peaks (cp1 and cp2), Figure 8a shows a three-color composite image using 4.5 μm (red), 3.6 μm (green), and 2.2 μm (blue), which is also overlaid with the 1.28 GHz emission. The source seen close to the peak cp1 is barely observed in the GPS K-band image. The source seen close to the peak cp2 is also observed in the GPS K-band image (position and JHK photometry: α_{2000} =18:03:01.38, δ_{2000} = −21:48:13.96; m$_J$ = 18.22$\pm$0.07 mag; m$_H$ = 17.39$\pm$0.08 mag; m$_K$ = 17.79$\pm$0.3 mag). In Figure 8b, we present the VLT/NACO adaptive-optics NIR images (H and K$_s$; below 8000 AU scale) toward the radio peaks (i.e. cp1 and cp2). A point-like source is seen toward each compact radio peak in the VLT/NACO images. There are no nebular features seen toward these sources in the NACO images.

High-resolution spectroscopic study will be very helpful to confirm the ionizing sources of the radio peaks.

3.5. *Young stellar objects*

3.5.1. *Study of identification of YSOs*

The study of YSO populations is a powerful tool to depict the picture of ongoing star formation activity in a given star-forming region. In this section, we identify and classify the YSO populations using their infrared excess for a wider field of view around IRAS 17599−2148. Previously, Dewangan et al. (2012) also presented the photometric analysis of point-like sources in the IRAS 17599−2148 region, which was restricted only near the bipolar nebula. In the following, we give a brief description of YSOs identification and classification

schemes adopted in this work.

1. In this scheme, the GLIMPSE-MIPSGAL color-magnitude diagram ([3.6]−[24]/[3.6]) is used to identify the different stages of YSOs (Guieu et al. 2010; Rebull et al. 2011; Dewangan et al. 2015b), where the sources have detections in the MIPSGAL 24 μm and GLIMPSE 3.6 μm bands. The 24 μm image is saturated near the IRAS position, therefore this scheme is not used to trace YSOs near the IRAS position (see Figure 1a). Following the conditions given in Guieu et al. (2010), the boundary of different stages of YSOs is also highlighted in Figure 9a. In our selected region, we find 170 sources that have detections in both the 3.6 and 24 μm bands. We identify 39 YSOs (4 Class I; 7 Flat-spectrum; 28 Class II) and 131 Class III sources. Furthermore, Figure 9a exhibits the boundary of possible contaminants (i.e. galaxies and disk-less stars) (also see Figure 10 in Rebull et al. 2011). We also find that our identified YSO populations are free from the contaminants. We also identify an embedded source in the IRDC, which is detected at wavelengths longer than 3.6 μm and is designated as MG008.2845+00.1664 in the MIPSGAL photometry catalog (Gutermuth & Heyer 2015). The source has 4.5–24 μm bands photometry and is a YSO candidate with a color ($m_{8.0}$ - m_{24}) of 3.54 mag.

2. In this scheme, the GLIMPSE color-color diagram ([3.6]−[4.5] vs [5.8]−[8.0]) of sources is employed that have detections in all four GLIMPSE bands. Following the Gutermuth et al. (2009) schemes, YSOs and various possible contaminants (e.g. broad-line active galactic nuclei (AGNs), PAH-emitting galaxies, shocked emission blobs/knots, and PAH-emission-contaminated apertures) are identified in our selected region. The possible contaminants are also removed from the selected YSOs. Furthermore, these YSOs are classified into different evolutionary stages based on their slopes of the *Spitzer*-GLIMPSE SED ($\alpha_{3.6-8.0}$) computed from 3.6 to 8.0 μm (i.e. Class I ($\alpha_{3.6-8.0} > -0.3$), Class II ($-0.3 > \alpha_{3.6-8.0} > -1.6$), and Class III ($-1.6 > \alpha_{3.6-8.0} > -2.56$)) (e.g., Lada et al. 2006). The GLIMPSE color-color diagram ([3.6]−[4.5] vs [5.8]−[8.0]) is shown in Figure 9b. More details on the YSO classifications can be found in the work of Dewangan & Anandarao (2011, and references therein). This scheme leads 15 YSOs (5 Class I; 10 Class II), 2282 photospheres, and 288 contaminants.

3. In this scheme, the color-color space ([4.5]−[5.8] vs [3.6]−[4.5]) of sources is used that have detections in the first three GLIMPSE bands (except 8.0 μm band). The color conditions, [4.5]−[5.8] $\geq$ 0.7 and [3.6]−[4.5] $\geq$ 0.7, are adopted to select protostars, as given in Hartmann et al. (2005) and Getman et al. (2007). 11 protostars are found in our selected region (see Figure 9c).

4. In this scheme, the color-magnitude space (H−K/K) is adopted for selecting additional YSOs. To find a color condition, we explored the color-magnitude space of the nearby control field (size $\sim 5' \times 5'$; central coordinates: $\alpha_{J2000} = 18^h02^m20^s.7$, $\delta_{J2000} = -21^\circ50'31''.1$) and selected a color H−K value (i.e. $\sim$2.2) that separates large H−K excess sources from the rest of the population. Considering this color H−K cut-off criterion, 409 embedded YSOs are identified in our selected region (see Figure 9d).

Finally, all these schemes give us a total of 474 YSOs in our selected region (as shown in Figure 1). The positions of all these YSOs are shown in Figure 10a. Several embedded sources are detected toward the elongated filamentary structure.

3.5.2. *Study of distribution of YSOs*

The spatial distribution of young stellar populations is often examined using their surface density analysis (e.g. Gutermuth et al. 2009; Bressert et al. 2010), which allow us to infer the young stellar clusters. Previously, using the nearest-neighbour (NN) technique, Dewangan et al. (2012) also obtained the surface density map of YSOs in the IRAS 17599−2148 region, which was studied only near the bipolar nebula. The surface density map can be generated by dividing the selected field using a regular grid and computing the surface density of YSOs at each grid point. The surface number density at the j^{th} grid point is defined by $\rho_j = (n-1)/A_j$ (e.g. Casertano & Hut 1985), where A_j represents the surface area defined by the radial distance to the $n = 6$ NN. Following this procedure, we generated the surface density map of all the selected 474 YSOs, using a $5''$ grid and 6 NN at a distance of 4.2 kpc. In Figure 10b, the resultant surface density contours of YSOs is presented. The contour levels are drawn at 4, 6, 9, 15, and 25 YSOs/pc^2, increasing from the outer to the inner regions. The YSOs clusters are mainly seen toward the IRDC and the bipolar nebula (see Figure 10b). The star formation activity is found toward all the condensations as traced in the *Herschel* column density map.

We also obtained the clustered populations from distributed sources using a statistical analysis of YSOs. We estimated an empirical cumulative distribution (ECD) of YSOs as a function of NN distance (see Chavarría et al. 2008; Gutermuth et al. 2009; Dewangan & Anandarao 2011, for more details). In the ECD analysis, a cutoff length (also referred as the distance of inflection d_c) is selected for delineating the low-density/distributed populations. For the present case, we selected a cutoff distance of $d_c \sim 44''$ (0.9 pc at a distance of 4.2 kpc). The ECD analysis provided a clustered fraction of about 72% YSOs (i.e. 344 from a total of 474 YSOs).

4. DISCUSSION

On a wider field of view around IRAS 17599−2148, an elongated filamentary structure (extension $\sim$21 pc) has been traced in the *Herschel* continuum images. In Section 3.1.1, we mentioned about the presence a continuous velocity structure in the direction of IRAS 17599−2148 and presented evidence of the existence of the elongated filamentary structure. Considering the molecular and ionized gas velocities, the elongated filamentary structure harbours the IRDC, and a bipolar nebula associated with the H II region IRAS 17599−2148/G8.14+0.23. The ATLASGAL sources at 870 μm (i.e., a chain of dense clumps/cores) are exclusively found toward the IRDC and the bipolar nebula, tracing dense regions qualitatively. In Section 3.2, using *Herschel* data analy-

sis, the physical conditions (column density and temperature) have been inferred in the region around IRAS 17599−2148. In the *Herschel* temperature map, the IRDC is traced with cold gas (without any radio detection), while the bipolar nebula is seen with warmer gas, indicating a temperature gradient. We found higher temperatures toward the waist of the bipolar nebula which is part of the H II region. This implies that the waist of the bipolar nebula is heated directly by massive stars that are embedded in dense gas as traced by NH_3 emission. Based on the temperature distribution in the *Herschel* temperature map, the bipolar nebula is clearly distinguished from the IRDC. This immediately suggests the presence of two distinct environments within the elongated filamentary structure. In our selected region, the *Herschel* column density map reveals twelve clumps. We find at least six massive clumps (IDs: 1–5 and 10; M_{clump} ∼777 – 7024 $M_{\odot}$) associated with the filamentary structure and two of them (IDs:1–2) are located at the waist of the bipolar nebula. Four additional clumps (IDs: 6–8 and 12) are also identified at the edges of the bipolar nebula. All the twelve clumps have higher self-gravitating pressure values (i.e. 2.1–29.2 × 10^{-10} dynes cm^{-2}) and smaller $t_{ff,sph}$ values (i.e. 0.4–0.77 Myr), indicating the signature of the early phase of star formation within the clumps. Based on availability of the line parameters toward four clumps (IDs:1–4), the virial parameters (M_{vir}/M_{clump}) for these clumps are less than 1, suggesting these clumps are prone to collapse. Based on availability of T_{kin}, two (IDs:1–2) out of these four clumps have higher Mach numbers (σ_{NT}/a_s) (i.e. 5 and 5.8), indicating that the clumps are dominated by non-thermal motions (such as outflows from YSOs). These clumps appear supersonic. All these results favour that the fragmentation occurred within the filaments, which leads several clumps with higher column densities. Indirectly, these clumps show the signatures of ongoing star formation activities.

In the era of ATLASGAL and *Herschel* surveys, the identification of elongated filaments and the formation of clumps in these filaments have received much attention (e.g. Schneider et al. 2012; Ragan et al. 2014; Contreras et al. 2016; Li et al. 2016, and references therein). The large-scale filaments are likely to be unstable to radial collapse and fragmentation. The spacing of the clumps in the filamentary cloud is often explained by the "sausage" instability produces during the gravitational collapse of a cylinder (Chandrasekhar & Fermi 1953; Nagasawa 1987). More recently, Contreras et al. (2016) studied fragmentation in five filamentary molecular clouds using data from the ATLASGAL 870 μm, *Spitzer*, and Millimetre Astronomy Legacy Team 90 GHz (MALT90) surveys and also suggested the observed separation of the clumps via the "sausage" instability theory. In this work, the presence of clumps (or a chain of dense clumps/cores) in the elongated filamentary structure could be explained by this instability theory. However, in order to validate the theoretical predictions, high-resolution molecular line data toward the elongated structure are required.

The distribution of YSOs clusters traces the star formation activities. In Section 3.5.2, the YSOs clusters are found toward the clumps in the elongated filamentary structure. The association of clumps and YSOs clusters is evident, illustrating further confirmation of star formation within the clumps. Additionally, the spatial distribution of YSOs clusters is also seen at the edges of the bipolar nebula. Considering the spatial locations of the clusters, star formation appears more intense toward the IRDC. Note that the IRDC contains many deeply embedded YSOs without any ionized emission. The ionized emission is exclusively associated with the most massive clump, which is located at the waist of the bipolar nebula. A bipolar appearance of IRAS 17599−2148 could be explained due to the ionizing feedback from the O6.5-O6 type star. The position-velocity analysis of the gas kinematics of CO(3–2) suggests the signature of an expanding H II region with an expansion velocity of the gas to be ∼4.5 km s^{-1}. Dewangan et al. (2012) estimated the dynamical or expansion age of the H II region to be ∼ 1.6 Myr. The average ages of Class I and Class II YSOs are estimated to be ∼0.44 Myr and ∼1–3 Myr (Evans et al. 2009), respectively. Hence, star formation in the clumps associated with the edges of the bipolar nebula could be influenced by the H II region. The H II region is spatially situated far away from the IRDC, therefore the star formation toward the IRDC is unlikely influenced by the H II region. This argument is also supported by the lower value of pressure of the H II region (i.e. $P_{HII} = \mu m_H c_s^2 \left(\sqrt{\frac{3N_{uv}}{4\pi\,\alpha_B\,D_s^3}}\right) \approx 8$–$5 \times 10^{-11}$ dynes cm^{-2}; where, μ = 2.37, c_s is the sound speed of the photo-ionized gas (= 10 km s^{-1}), and α_B is the radiative recombination coefficient (= 2.6 × 10^{-13} cm^3 s^{-1})) driven by an O6.5-O6 type star at projected distances (D_s) of 8–11 pc, which is very close to P_{MC}. The onset stellar cluster formation associated with the IRDC appears to be spontaneous. Combining these results, we notice that the different star formation processes have taken place in the bipolar nebula and the IRDC. The star formation associated with the H II region is likely more evolved compared to the IRDC.

5. SUMMARY AND CONCLUSIONS

The present work deals with a multi-scale and multi-wavelength analysis around IRAS 17599−2148, using new observations along with publicly available archival datasets. The goal of this paper is to understand the physical environment and star formation processes around IRAS 17599−2148 on the smaller and larger scales. In the following, the important results of this work are provided.

- On a larger scale, an elongated filamentary structure is evident in the *Herschel* images, which hosts the IRDC and the H II region IRAS 17599−2148/G8.14+0.23. IRAS 17599−2148 has a bipolar appearance at wavelengths longer than 2 μm. Radio emission is not detected toward the IRDC.
- High-resolution GMRT radio continuum emissions at 0.61 GHz (beam size ∼5″.6 × 5″.2) and 1.28 GHz (beam size ∼2″.8 × 2″.4) show an extended radio emission, which is located toward the waist of the bipolar nebula and can be excited by a single star of radio spectral type, O6.5–O6.
- The 1.28 GHz map reveals two radio continuum peaks (cp1 and cp2) toward the single peak seen in the 0.61

GHz map. The radio peaks, cp1 and cp2 corresponds to a single ionizing star of radio spectral type, O8V–O8.5V and O9V–O9.5V, respectively.

• Within a 18″ of the IRAS 17599−2148 position, two radio O-spectral type sources and a 6.7 GHz MME (without any radio peak) are traced, indicating the presence of different early evolutionary stages of massive star formation.

• IRS 1 has been identified as an IRc of the 6.7-GHz MME and is a massive protostar candidate. The GMRT radio continuum map at 1.28 GHz (1σ ∼0.38 mJy beam^{-1}) does not trace any radio peak toward IRS 1.

• The inner circumstellar environment of IRS 1 is mapped using the VLT/NACO adaptive-optics K_s and L′ observations at resolutions ∼0.″2 and ∼0.″1, respectively. Within a scale of 4200 AU, IRS 1 has been resolved into at least three point-like sources and one of them is associated with diffuse emission, which could be a collimated infrared jet.

• Multi-scale and multi-wavelength data suggest that IRS 1 could be a genuine massive protostar candidate in a very early evolutionary stage, prior to an UCH II phase. Further detailed studies of IRS 1 are encouraged using high-resolution interferometric observations at longer wavelength.

• The *Herschel* column density map traces twelve clumps and their masses vary between 410 $M_\odot$ and 7024 $M_\odot$. In the selected region around IRAS 17599−2148, these clumps are identified with a range of temperature and column density of about 16–39 K and 0.6–11 × 10^{22} cm^{-2} (A_V ∼7–117 mag), respectively.

• The elongated filamentary structure is associated with at least six massive condensations, indicating the fragmentation of the cloud. This argument is also supported by virial analysis of clumps and their higher values of self-gravitating pressure. The most massive condensation (mass ∼7024 $M_\odot$) hosts two radio continuum peaks and the 6.7 GHz MME, which is located at the waist of the bipolar nebula. At least four condensations are also found at the edges of the bipolar nebula.

• In the *Herschel* temperature map, the IRDC is found with cold gas (and the absence of any radio continuum emission), while the bipolar nebula is associated with warmer gas and is part of the H II region. Based on the temperature distribution and ionized emission, the bipolar nebula is clearly distinguished from the IRDC. This implies two distinct environments within the elongated filamentary structure.

• The position-velocity analysis of the gas kinematics of CO(3–2) suggests the signature of an expanding H II region with an expansion velocity of the gas to be ∼4.5 km s^{-1};

• In the position-velocity plot of CO(3–2), a noticeable velocity gradient has also been found toward the IRAS 17599−2148 position, indicating the presence of a molecular outflow. The exciting source of the outflow could be the driving source of the H II region and/or the IRc of the 6.7 GHz MME, however, due to coarse beam of CO data, we cannot conclude the powering source of the molecular outflow in this work.

• The analysis of the MIPSGAL, GLIMPSE, and UKIDSS-GPS photometry reveals a total of 474 YSOs. The YSOs clusters are spatially seen toward the condensations in the filamentary structure, revealing ongoing star formation. YSOs are also identified at the edges of the bipolar nebula.

• A point-like source is seen toward each compact radio continuum peak in the VLT/NACO images. There are no nebular features seen toward these sources in the NACO images. High-resolution spectroscopic study will be very helpful to confirm the ionizing sources of the radio peaks.

Based on our observed results, we conclude that the fragmentation has been occurred within the elongated filamentary structure, which produced several clumps (or a chain of dense clumps/cores) along the structure. Star formation activities are going on within these clumps. These YSOs might have spontaneously formed due to processes not related to the expanding H II region. Massive stars were formed in one of the highest column density and massive clumps, and subsequently, an H II region was originated. This H II region has also been expanded in the surroundings and its ionizing feedback formed a bipolar nebula. At the edges of the bipolar nebula, four additional clumps are also associated with the YSOs clusters. The expanding H II region may also have triggered the star formation in the periphery of the nebula.

We thank the anonymous referee for providing the constructive comments. The research work at Physical Research Laboratory is funded by the Department of Space, Government of India. This work is based on data obtained as part of the UKIRT Infrared Deep Sky Survey. This publication made use of data products from the Two Micron All Sky Survey (a joint project of the University of Massachusetts and the Infrared Processing and Analysis Center / California Institute of Technology, funded by NASA and NSF), archival data obtained with the *Spitzer* Space Telescope (operated by the Jet Propulsion Laboratory, California Institute of Technology under a contract with NASA). We thank the staff of the GMRT that made the radio observations possible. The GMRT is run by the National Centre for Radio Astrophysics of the Tata Institute of Fundamental Research. IZ is supported by the Russian Foundation for Basic Research (RFBR). AL acknowledges the CONACYT(México) grant CB-2012-01-1828-41.

REFERENCES

Arce, H. G., Borkin, M. A., Goodman, A. A., Pineda, J. E.,& Beaumont, C. N. 2011, ApJ, 742, 105
Baug, T., Ojha, D. K., Dewangan, L. K., et al. 2015, MNRAS, 454, 4335
Becker,R. H., White, R. L., Helfand, D. J., & Zoonematkermani, S. 1994, ApJS, 91,347
Benjamin, R. A.,Churchwell, E., Babler, B. L., et al. 2003, PASP, 115, 953
Beuther, H., Ragan, S. E., Johnston, K., et al. 2015, A&A, 584, 67
Bohlin, R. C., Savage, B. D., & Drake, J. F. 1978, ApJ, 224, 13233
Bressert, E., Bastian, N., Gutermuth, R., et al. 2010, MNRAS, 409, 54
Carey, S. J., Noriega-Crespo, A., Price, S. D., et al. 2005, BAAS, 37, 1252
Casali, M., Adamson, A., Alves de Oliveira, C., et al. 2007, A&A, 467, 777

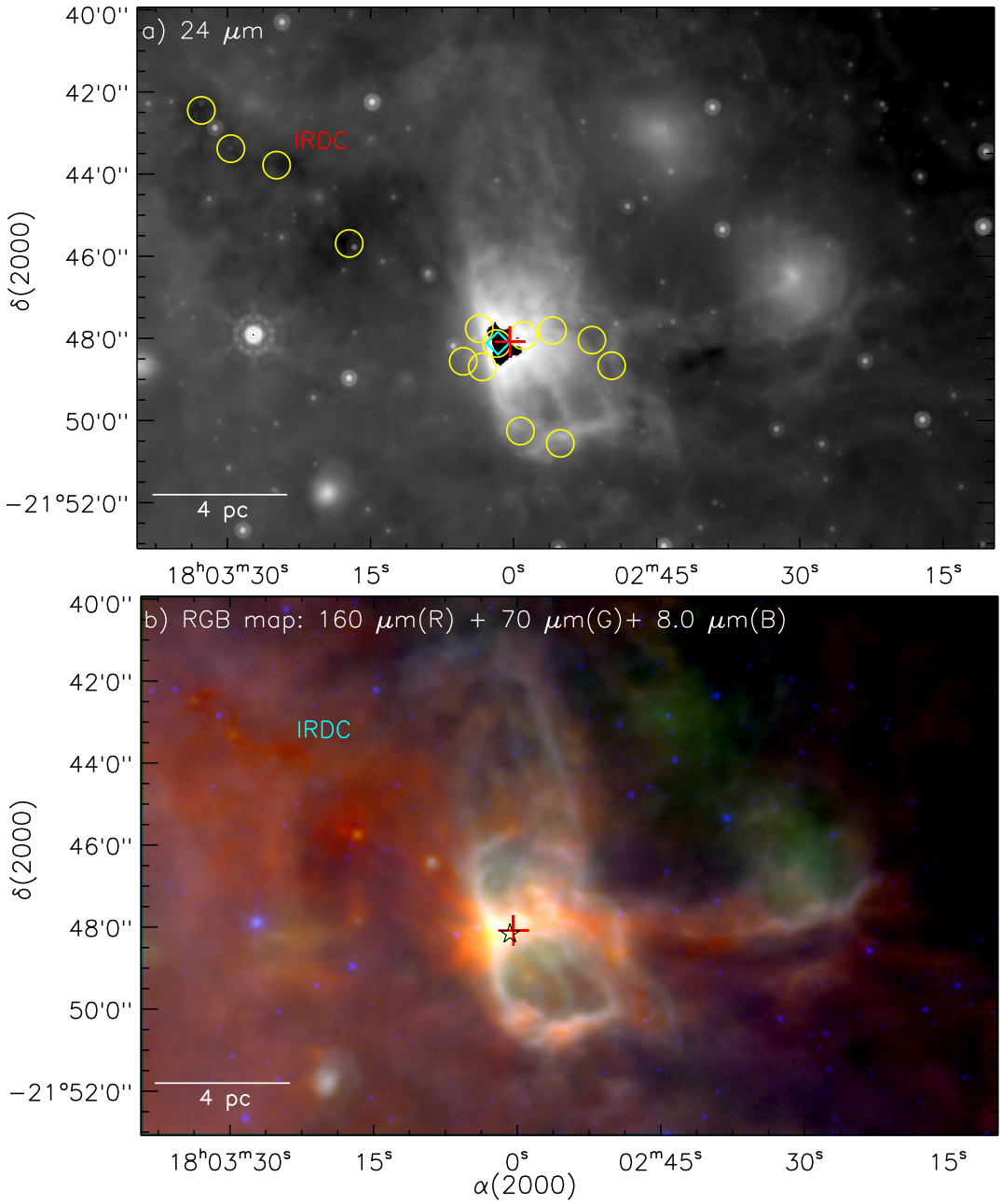

Figure 1. Distribution of the MIR and FIR emission toward the region around IRAS 17599−2148 (size of the selected region ∼20′.8 × 13′.2 (∼25.4 pc × 16.1 pc at a distance of 4.2 kpc); centered at $\alpha_{2000} = 18^h02^m54.5^s$, $\delta_{2000} = -21°46'33''.6$). a) The MIPSGAL 24 μm image of the region probed in this paper. A diamond symbol shows the VLA 6 cm (5 GHz) radio detection (Becker et al. 1994). The 24 μm image is saturated near the radio detection. The ATLASGAL clumps at 870μm (Contreras et al. 2013) are also marked by yellow circles. b) The image is the result of the combination of three bands: 160 μm (red), 70 μm (green), and 8.0 μm (blue). A star symbol indicates the position of the 6.7-GHz MME. In both the panels, the position of IRAS 17599−2148 (+) is marked. The scale bar corresponding to 4 pc (at a distance of 4.2 kpc) is shown in both panels. The images have revealed an IRDC (Simon et al. 2006) and a bipolar nebula (Dewangan et al. 2012).

Casertano, S., & Hut P. 1985, ApJ, 298, 80
Chandrasekhar, S., & Fermi E. 1953, ApJ, 118, 116
Chavarría, L. A., Allen, L. E., Hora, J. L., Brunt, C. M., & Fazio, G. G. 2008, ApJ, 682, 445
Churchwell, E., Watson, D. F., Povich, M. S., et al. 2007, ApJ, 670, 428
Contreras Y., Schuller F., Urquhart J. S., et al., 2013, A&A, 549, 45
Contreras, Y., Garay, G., Rathborne, J. M., & Sanhueza,P. 2016, MNRAS, 456, 2041
Deharveng, L., Schuller, F., Anderson, L. D., et al. 2010, A&A, 523, 6
de Villiers, H. M., Chrysostomou, A., Thompson, M. A., et al. 2015, MNRAS, 449, 119
Dewangan, L. K., & Anandarao, B. G 2011, MNRAS, 414, 1526
Dewangan, L. K., Ojha, D. K., Anandarao, B. G., Ghosh, S. K., & Chakraborti, S. 2012, ApJ, 756, 151
Dewangan, L. K., Ojha, D. K., Grave, J. M. C., & Mallick, K. K. 2015a, MNRAS, 446, 2640
Dewangan, L. K., Luna, A., Ojha, D. K., et al. 2015b, ApJ, 811, 79
Dewangan, L. K., Ojha, D. K., Luna, A., et al. 2016, ApJ, 819, 66
Duchêne, G., & Kraus, A., ARA&A 2013, 51, 269
Dunham, M. K., Rosolowsky, E., Evans, II N. J., Cyganowski, C., & Urquhart, J. S. 2011, ApJ, 741, 110

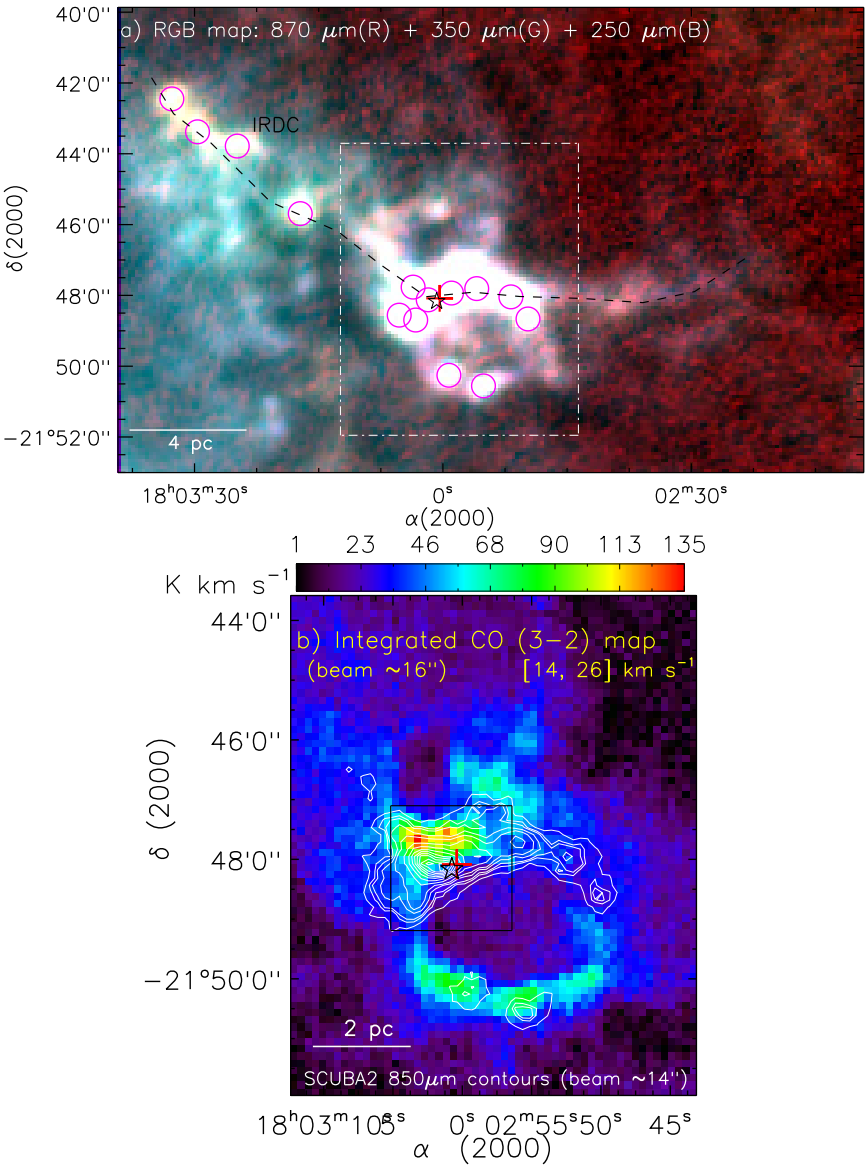

Figure 2. a) Three-color composite image (*red*, ATLASGAL 870 μm; *green*, *Herschel* 350 μm; *blue*,*Herschel* 250 μm; in linear scale) of the region around IRAS 17599−2148, which clearly traces the cold dust emission. An elongated filamentary structure is highlighted by a dashed curve. The ATLASGAL clumps at 870μm (Contreras et al. 2013) are also marked by magenta circles. The faint dust emissions (or infrared bridges) traced in the *Herschel* images are also found between the ATLASGAL clumps, indicating that this chain of dense clumps/cores belongs to a single entity (i.e., elongated filamentary structure; see a dashed curve) (also see text for details). The dotted-dashed white box encompasses the area shown in Figure 2b. The scale bar at the bottom-left corner corresponds to 4 pc (at a distance of 4.2 kpc). b) Integrated CO (3–2) emission map overlaid with the SCUBA-2 850 μm contours. The 850 μm contours are superimposed with levels of 4, 8, 10, 15, 20, 30, 40, 50, 60, 70, 80, 90, and 97% of the peak value (i.e., 15.5 mJy/arcsec^2). The figure shows the distribution of molecular gas and dense materials in the region around IRAS 17599−2148. The solid black box encompasses the area shown in Figure 3. The scale bar at the bottom-left corner corresponds to 2 pc (at a distance of 4.2 kpc). In both the panels, the marked symbols are similar to those shown in Figure 1.

Dyson, J. E., & Williams, D. A. 1980, Physics of the interstellar medium, New York, Halsted Press, 204 p

Evans, N. J., II, Dunham, M. M., Jørgensen, J. K., et al. 2009, ApJS, 181, 321

Flaherty, K. M., Pipher, J. L., Megeath, S. T., et al. 2007, ApJ, 663, 1069

Getman, K. V., Feigelson, E. D., Garmire,G., Broos, P., & Wang, J. 2007, ApJ, 654, 316

Goto, M., Stecklum, B., Linz, H., et al. 2006, ApJ, 649, 299

Griffin, M. J., Abergel, A., Abreu, A, et al. 2010, A&A, 518L, 3

Guieu, S., Rebull, L. M., Stauffer, J. R., et al. 2010, ApJ, 720, 46

Gutermuth, R. A., Megeath, S. T., Myers, P. C., et al. 2009, ApJS, 184, 18

Gutermuth, R. A., & Heyer, M. 2015, AJ, 149, 64

Hartmann, L., Megeath, S. T., Allen, L., et al. 2005, ApJ, 629, 881

Hildebrand, R. H. 1983, Quarterly Journal of the RAS, 24, 267

Kauffmann, J., Bertoldi, F., Bourke, T. L., Evans, II, N. J.,& Lee, C. W. 2008, ApJ, 487, 993

Kim, K. T., & Koo, B. C 2001, ApJ, 549, 979

Lada, C. J., Muench, A. A., Luhman, K. L., et al. 2006, AJ, 131, 1574

Lawrence, A., Warren, S. J., Almaini, O., et al. 2007, MNRAS, 379, 1599

Lenzen, R., Hartung, M., Brandner, W., et al. 2003, Proc. SPIE, 4841, 944

Li, Guang-Xing, Urquhart, J. S., Leurini, S., et al. 2016, A&A, 591, 5

Lucas, P. W., Hoare, M. G., Longmore, A., et al. 2008, MNRAS, 391, 1281

MacLaren, I., Richardson, K. M., & Wolfendale, A. W. 1988, ApJ, 333, 821

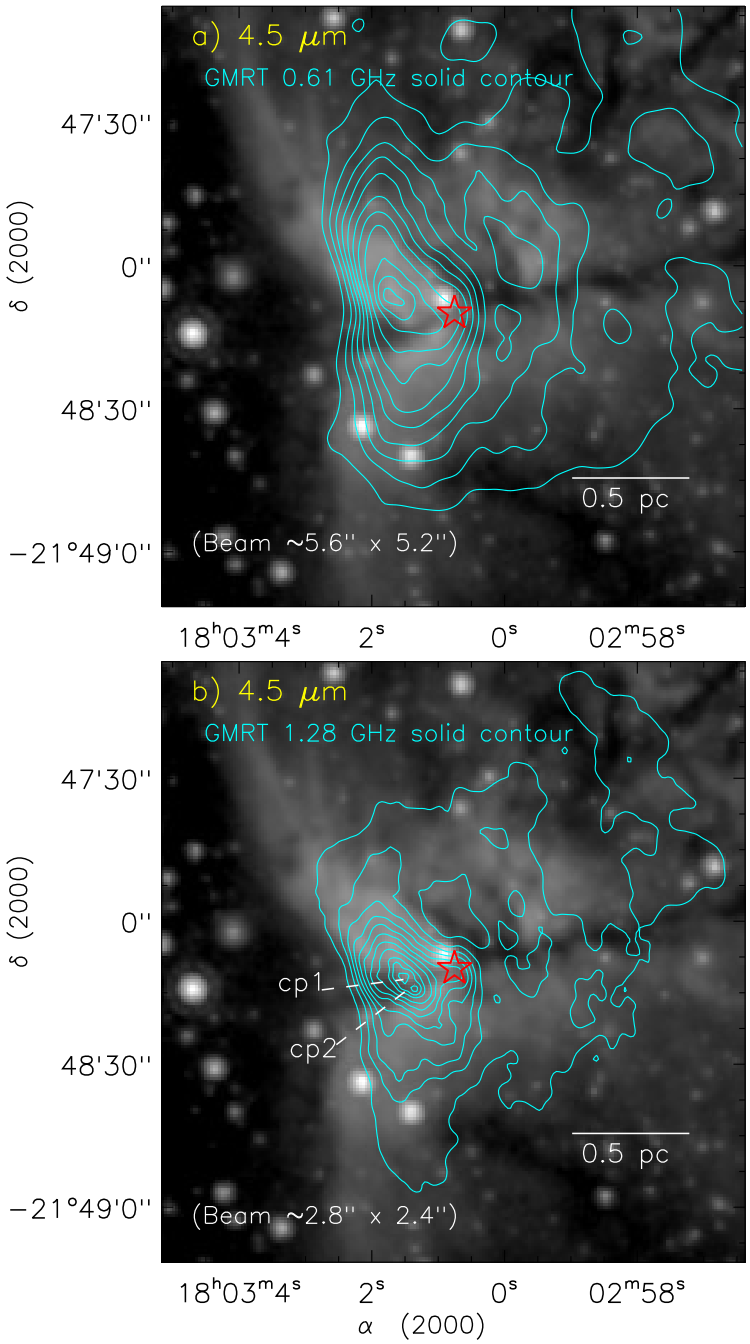

Figure 3. High-resolution GMRT radio continuum emissions at 0.61 GHz (beam size ∼5.″6 × 5.″2) (a) and 1.28 GHz (beam size ∼2.″8 × 2.″4) (b). In each panel, the radio contours are overlaid on the 4.5 μm image. The 1.28 GHz map traces two compact peaks (i.e. cp1 and cp2), which are also labeled in the bottom panel. In both the panels, the contours are overlaid with levels of 10, 20, 30, 40, 50, 60, 70, 80, 90, 95, and 99% of the peak values (i.e. 0.0738 Jy/beam for 0.61 GHz; 0.0225 Jy/beam for 1.28 GHz). In both the panels, a star symbol indicates the position of the 6.7-GHz MME. In both the panels, the scale bar at the bottom-right corner corresponds to 0.5 pc (at a distance of 4.2 kpc).

Mallick, K. K., Ojha, D. K., Samal, M. R., et al. 2012, ApJ, 759, 48
Mallick, K. K., Kumar, M. S. N., Ojha, D. K., et al. 2013, ApJ, 779, 113
Mallick, K. K., Ojha, D. K., Tamura, M., et al. 2015, MNRAS, 447, 2307
Martins, F., Schaerer, D., & Hillier, D. J. 2005, A&A, 436, 1049
Matsakis, D. N., Evans, N. J., II, Sato, T., & Zuckerman, B. 1976, AJ, 81, 172
Minier, V., Conway, J. E., & Booth, R. S. 2001, A&A, 369, 278
Nagasawa M., 1987, Progress of Theoretical Physics, 77, 635
Omar, A., Chengalur, J. N., & Anish Roshi, D. 2002, A&A, 395, 227
Ott, S. 2010, in Astronomical Society of the Pacic Conference Series, Vol. 434, Astronomical Data Analysis Software and Systems XIX, ed. Y. Mizumoto, K.-I. Morita, & M. Ohishi, 139
Poglitsch, A., Waelkens, C., Geis, N., et al. 2010, A&A, 518L, 2
Rathborne, J. M., Garay, G., Jackson, J. M., et al. 2011, ApJ, 741, 120
Ragan,S. E., Henning, Th., Tackenberg, J., et al. 2014, A&A, 568, 73
Ragan, S. E., Henning, T., Beuther, H., Linz, H., & Zahorecz, S. 2015, A&A, 573, 119
Rebull, L. M., Guieu, S., Stauffer, J. R., et al. 2011, ApJS, 193, 25
Rousset, G., Lacombe, F., Puget, P., et al. 2003, Proc. SPIE, 4839, 140

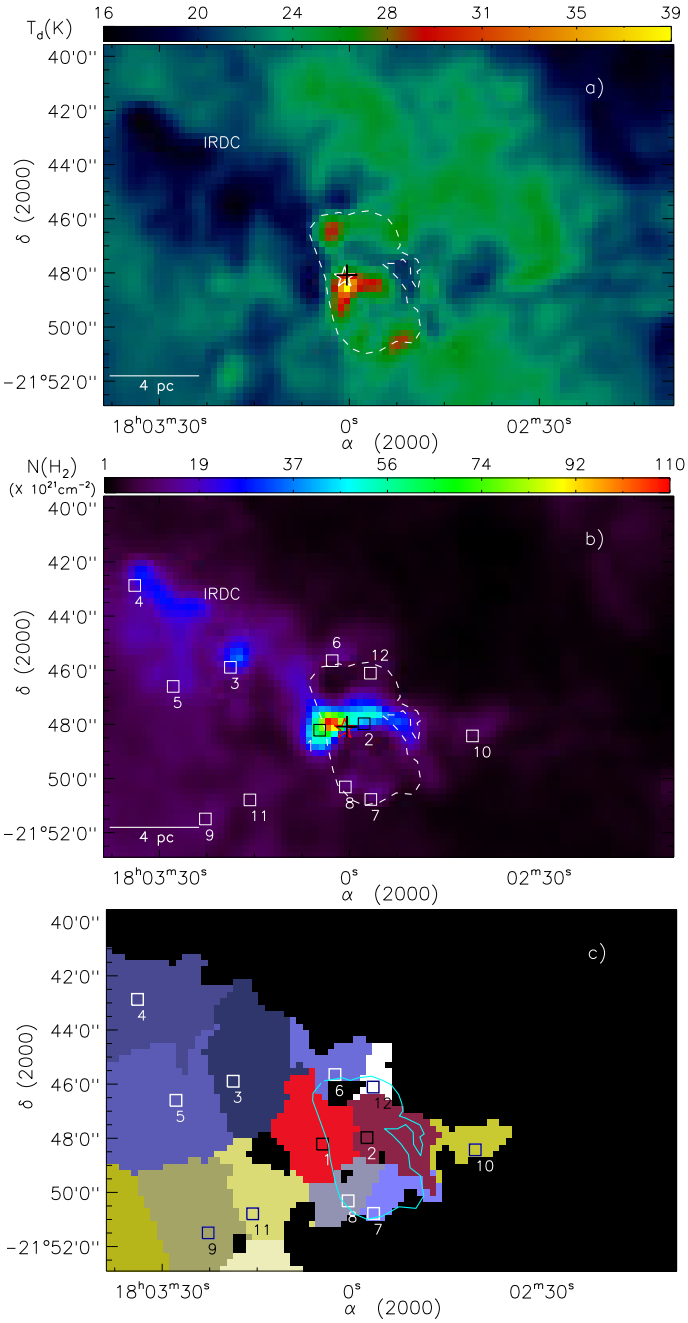

Figure 4. *Herschel* temperature map (a) and column density ($N(H_2)$) map (b) of the region around IRAS 17599−2148 (see text for details). The column density map allows to infer the extinction with $A_V = 1.07 \times 10^{-21}\ N(H_2)$ and to identify the clumps (see text for details). The identified clumps are marked by square symbols and the boundaries of these clumps are shown in Figure 4c (also see Table 1). c) The boundary of each identified clump is highlighted along with its corresponding clump ID (see Table 1 and also Figure 4b). A bipolar nebula is depicted from the *Spitzer* 8 μm emission (see Dewangan et al. 2012), which is shown in all the panels. In the first two panels, the other marked symbols are similar to those shown in Figure 1. In the first two panels, the scale bar at the bottom-right corner corresponds to 4 pc (at a distance of 4.2 kpc).

Schneider, N., Csengeri, T., Hennemann, M., et al. 2012, A&A, 540, L11

Schuller, F., Menten, K. M., Contreras, Y., et al. 2009, A&A, 504, 415

Shirley, Y. L., Ellsworth-bowers, T. P., Svoboda, B., et al. 2013, ApJS, 209, 2

Simon, R., Jackson, J. M., Rathborne, J. M., & Chambers, E. T. 2006, ApJ, 639, 227

Skrutskie, M. F., Cutri, R. M., Stiening, R., et al. 2006, AJ, 131, 1163

Szymczak, M., Wolak, P., Bartkiewicz, A., & Borkowski, K. M. 2012, AN, 333, 634

Tackenberg, J., Beuther, H., Henning, T., et al. 2012, A&A, 540, 113

Takeuchi, T., Yamamoto, H., Torii, K., et al. 2010, PASJ, 62, 557

Tafalla, M., & Hacar, A. 2015, A&A, 574, 104

Tan, J. C., Beltrán, M. T., et al. 2014, aXriv 1402.0919

Tobin, J. J., Looney, L. W., Li, Zhi-Yun, et al. 2016, arXiv160100692

Urquhart, J. S., Moore, T. J. T., Schuller, F., et al. 2013, MNRAS, 431, 1752

Walsh, A. J., Burton, M. G., Hyland, A. R., & Robinson, G. 1998, MNRAS, 301, 640

Wienen, M., Wyrowski, F., Schuller, F., et al. 2012, A&A, 544, 146

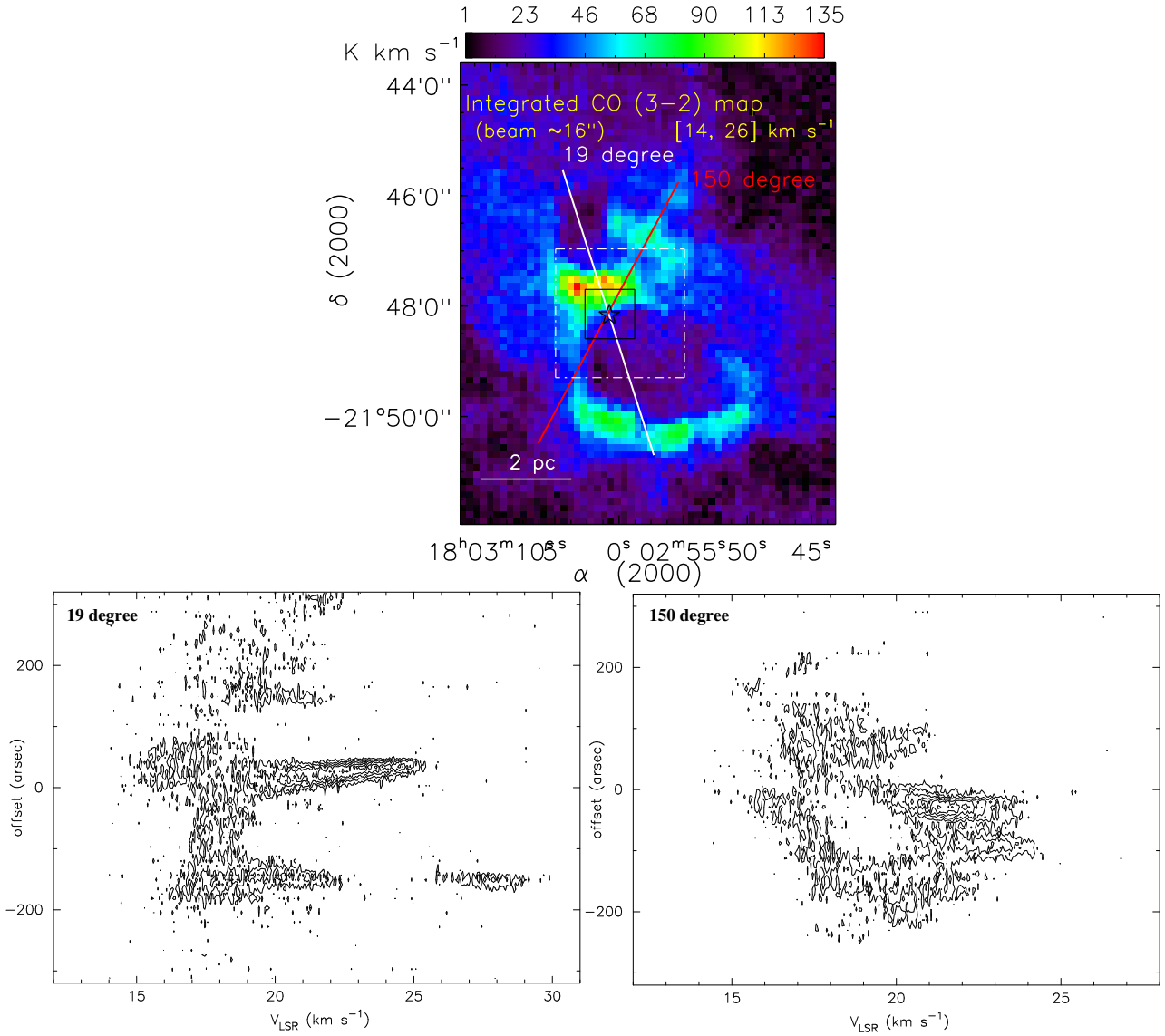

Figure 5. Top panel: Integrated CO (3–2) emission map of the region around IRAS 17599−2148, similar as shown in Figure 2b. Two solid lines with different position angles represent the axes, where the position-velocity diagrams are extracted. A star symbol indicates the position of the 6.7-GHz MME. The scale bar at the bottom-left corner corresponds to 2 pc (at a distance of 4.2 kpc). The dotted-dashed white box is shown as a zoomed-in view in Figure 6a. The solid black box is shown as a zoomed-in view in Figure 8a. **Bottom Left:** Position-velocity diagram along the axis with a position angle of 19° (see top panel in Figure 5). **Bottom Right:** Position-velocity diagram along the axis with a position angle of 150° (see top panel in Figure 5). In both the bottom panels, the offset reference is the position of the 6.7-GHz MME. The position-velocity diagrams show a C-like and a ring-like structure of gas, indicating the expanding shell with an expanding gas velocity of ∼4.5 km s^{-1}.

Williams, J. P., de Geus, E. J., & Blitz, L. 1994, ApJ, 428, 693
Xu, Jin-Long, Li, Di, Zhang, Chuan-Peng, et al. 2016, ApJ, 819,117
Zhang, Y., & Tan, J. C. 2011, ApJ, 733, 55
Zinnecker, H., & Yorke, H. W. 2007, ARA&A, 45, 481

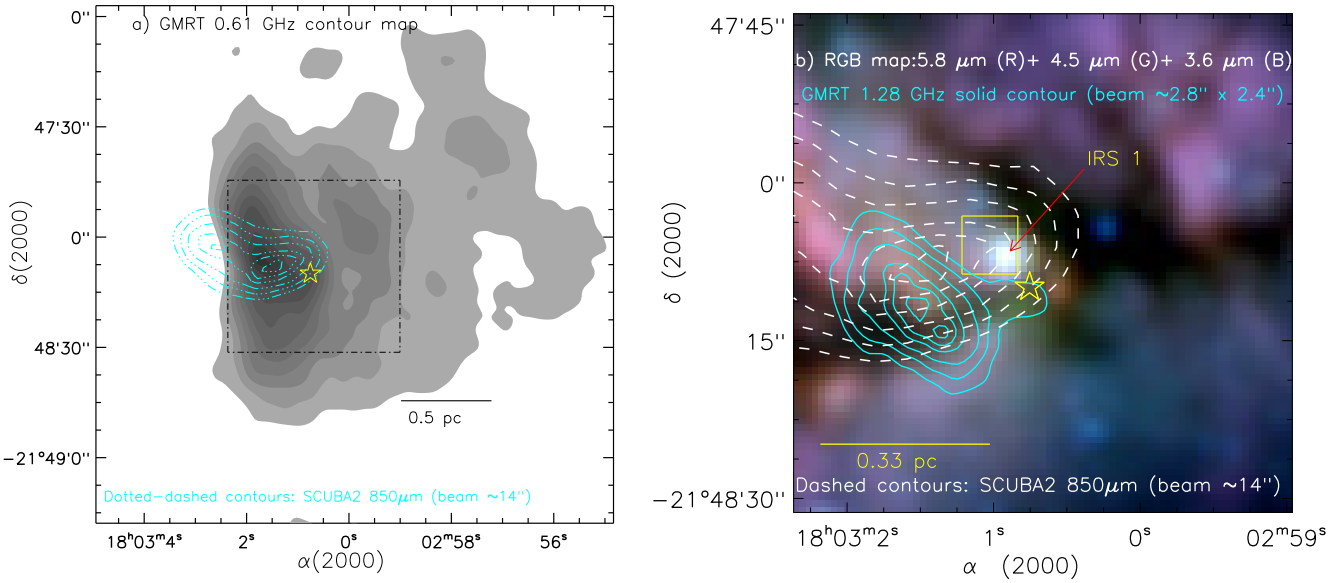
a) GMRT 0.61 GHz contour map
0.5 pc
Dotted−dashed contours: SCUBA2 850μm (beam ~14'')
δ(2000)
α(2000)
b) RGB map:5.8 μm (R)+ 4.5 μm (G)+ 3.6 μm (B)
GMRT 1.28 GHz solid contour (beam ~2.8'' x 2.4'')
IRS 1
0.33 pc
Dashed contours: SCUBA2 850μm (beam ~14'')
δ (2000)
α (2000)

Figure 6. a) The radio continuum contour map at 0.61 GHz is overplotted with contours of 850 μm emission (see dotted-dashed contours). The 0.61 GHz contours are shown with similar levels as shown in Figure 3a. The dotted-dashed black box encompasses the area shown in Figure 6b. The scale bar at the bottom-right corner corresponds to 0.5 pc (at a distance of 4.2 kpc). The figure shows the distribution of ionized and dust continuum emissions. b) Three-color composite image (*red*, 5.8 μm; *green*, 4.5 μm; *blue*, 3.6 μm; in log scale) of the region around IRS 1. The 1.28 GHz emission is also overlaid by contours with levels of 60, 70, 80, 90, 95, and 99% of the peak value (i.e. 0.0225 Jy/beam). IRS 1, previously reported by Dewangan et al. (2012), appears the reddest and brightest in the *Spitzer* images, and is located close to the sub-mm emission peak as well as the Class II 6.7 GHz MME position. The solid yellow box is shown as a zoomed-in view in Figures 7a, 7b, and 7c. The scale bar at the bottom-left corner corresponds to 0.33 pc (at a distance of 4.2 kpc). In both the panels, the 850 μm emission is also overlaid by contours with levels of 60, 70, 80, 90, 95, and 99% of the peak value (i.e., 15.5 mJy/arcsec^2). In both the panels, the position of the 6.7-GHz MME is marked with a star symbol.

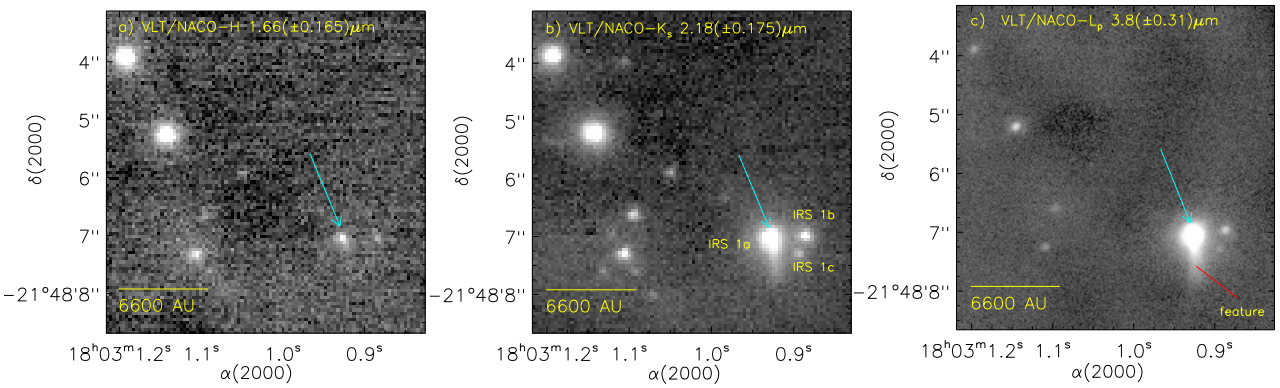

Figure 7. The VLT/NACO adaptive-optics H, K$_s$, and L$'$ images of the region around IRS 1 (in log scale). The selected area of the VLT/NACO images is shown by a solid box in Figure 6b. In each panel, the position of a resolved point-like source ($\alpha_{2000} = 18^h03^m00^s.93$, $\delta_{2000} = -21°48'07''.05$) is highlighted by an arrow. In each panel, the scale bar at the bottom-left corner corresponds to 6600 AU (at a distance of 4.2 kpc). The NACO images have resolved IRS 1 into at least three point-like sources (labeled as IRS 1a, 1b, and 1c) and one of them is associated with a diffuse emission feature within a scale of 4200 AU.

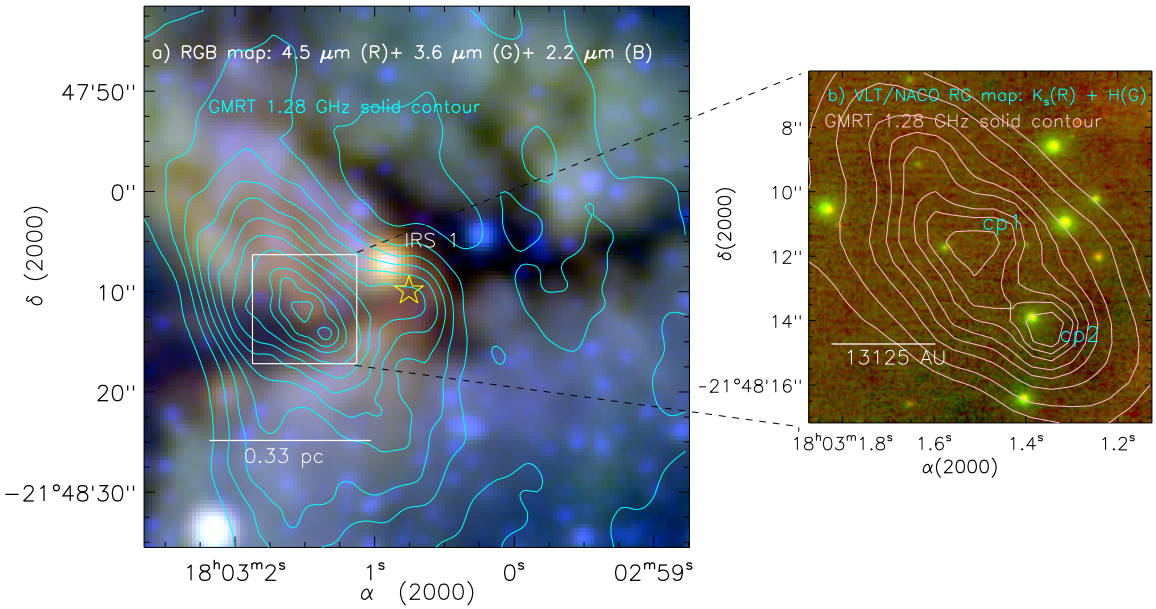

Figure 8. a) Three-color composite image (*red*, 4.5 μm; *green*, 3.6 μm; *blue*, 2.2 μm; in log scale) of the region around IRS 1. The 1.28 GHz emission is also overlaid by contours with similar levels as shown in Figure 3b. The solid white box encompasses the area shown in Figure 8b. A star symbol indicates the position of the 6.7-GHz MME. The scale bar at the bottom-left corner corresponds to 0.33 pc (at a distance of 4.2 kpc). b) The VLT/NACO two-color composite image (*green*, H-band; *red*, K_s-band; in log scale) of the region around the radio compact peaks. The selected area of the VLT/NACO images is shown by a box in Figure 8a, tracing the small-scale environment. The 1.28 GHz radio contours are also overlaid with levels of 80, 85, 90, 93, 95, 97, 98, and 99% of the peak value (i.e. 0.0225 Jy/beam). The scale bar at the bottom-left corner corresponds to 13125 AU (at a distance of 4.2 kpc). In the VLT/NACO images, a point-like source (without any diffuse emission) is seen toward each radio peak.

Table 1

Summary of the properties of the identified *Herschel* clumps within the region probed in this paper using the *Herschel* data (see Figures 4b and 4c). Column 1 lists the IDs given to the clump. Table also contains positions, deconvolved effective radius (R_c), clump mass (M_{clump}), self-gravitating pressure ($P_{clump} \approx \pi G(M_{clump}/\pi R_c^2)^2$), spherical free-fall time ($t_{ff,sph} \approx 16.6(R_c/pc)^{3/2}(M_{clump}/M_\odot)^{-1/2}$), peak velocity ($V_{peak}$), line-width ($\Delta V$), and virial mass ($M_{vir} = 126\, R_c\, \Delta V^2$).

ID	RA [J2000]	Dec [J2000]	R_c[a] (pc)	M_{clump} ($M_\odot$)	P_{clump} (10^{-10} dynes cm^{-2})	$t_{ff,sph}$ (Myr)	V_{peak} (km s^{-1})	ΔV (km s^{-1})	M_{vir} ($M_\odot$)
1	18:03:04.7	−21:48:13.0	2.0	7023.7	29.2	0.39	18.6[b]	3.36[b]	2830
2	18:02:57.7	−21:47:58.6	1.8	4147.6	14.8	0.47	18.58[b]	3.39[b]	2625
3	18:03:18.8	−21:45:53.6	2.5	5454.5	6.9	0.57	18.7[c]	3.1[c]	3047
4	18:03:33.9	−21:42:52.2	2.5	6418.6	9.6	0.52	18.9[c]	2.7[c]	2306
5	18:03:27.8	−21:46:36.0	2.9	6422	5.5	0.60	–	–	–
6	18:03:02.7	−21:45:38.9	1.4	1192.6	3.6	0.66	–	–	–
7	18:02:56.6	−21:50:46.5	1.2	763.8	3.0	0.70	–	–	–
8	18:03:00.6	−21:50:18.7	1.4	1046.2	2.8	0.70	–	–	–
9	18:03:22.7	−21:51:29.7	2.4	3377.9	3.3	0.70	–	–	–
10	18:02:40.6	−21:48:25.7	1.2	776.8	2.3	0.74	–	–	–
11	18:03:15.7	−21:50:47.4	1.8	1678.5	2.5	0.73	–	–	–
12	18:02:56.7	−21:46:06.6	0.9	410	2.1	0.76	–	–	–

[a] It is estimated using *clumpfind* algorithm.
[b] NH_3(1,1) derived line parameters from Wienen et al. (2012).
[c] HCO^+(3–2) derived line parameters from Shirley et al. (2013).

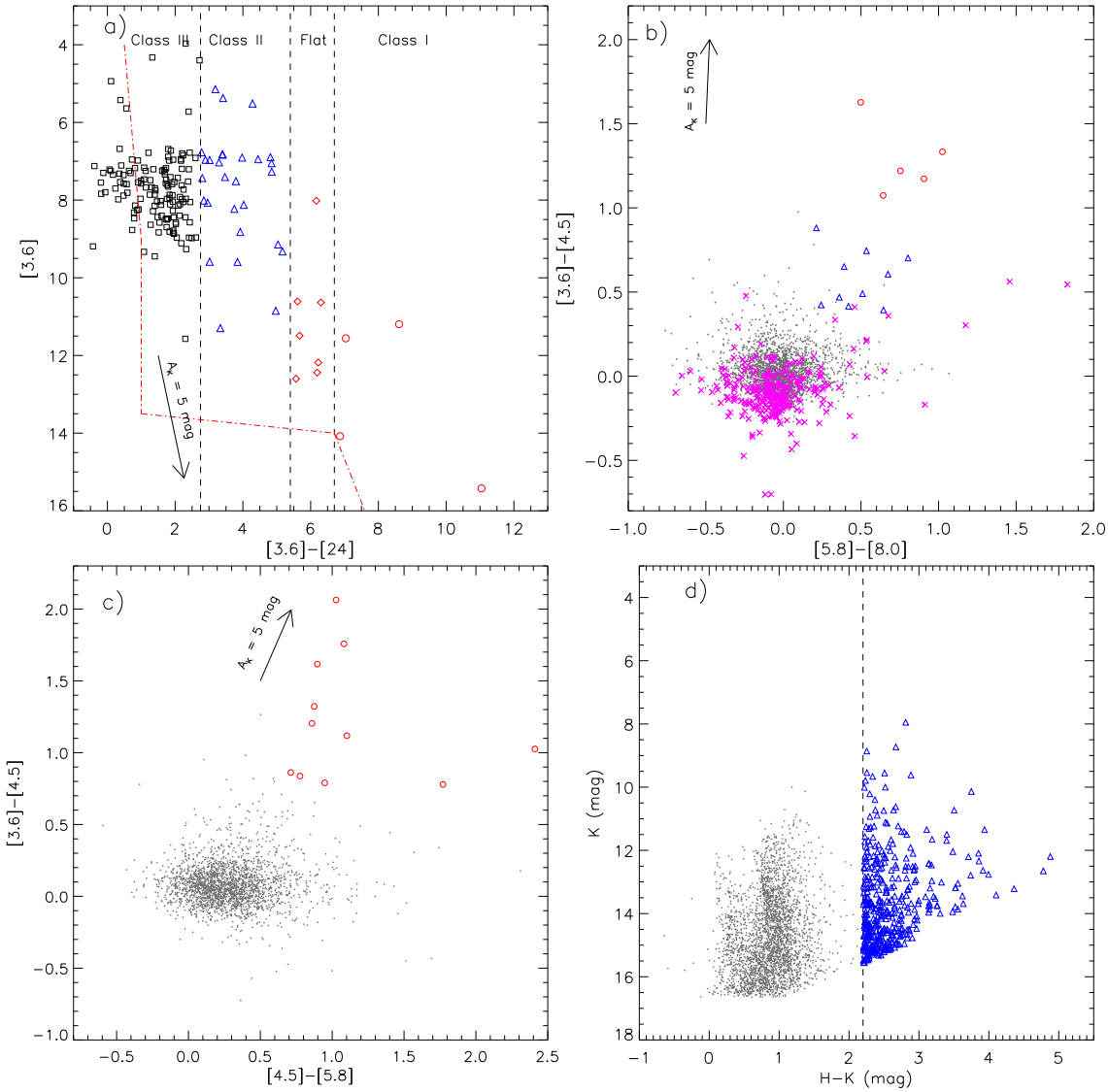

Figure 9. Selection of embedded young stellar population within the region probed in this paper (see Figure 2). a) Color-magnitude diagram ([3.6] − [24] vs [3.6]) showing the YSOs belonging to different evolutionary stages (see dashed lines). These sources are detected in the GLIMPSE 3.6 μm and the MIPSGAL 24 μm bands (see the text for more details). The YSOs and contaminated candidates (galaxies and disk-less stars) are separated by a dotted-dashed curve (see Rebull et al. 2011, for more details). The Flat-spectrum and Class III sources are designated by "◇" and "□" symbols, respectively; b) Color-color diagram ([3.6]−[4.5] vs. [5.8]−[8.0]) of sources detected in the four GLIMPSE bands. The "×" symbol shows the PAH-emission-contaminated apertures (see the text); c) Color-color diagram ([3.6]−[4.5] vs. [4.5]−[5.8]) using the first three GLIMPSE band detections (except 8.0 μm image); d) Color-magnitude diagram (H−K/K) of the sources observed in the NIR bands. In all the panels, Class I and Class II YSOs are marked by red circles and open blue triangles, respectively. In the last three panels, the dots in gray color refer the stars with only photospheric emissions. In the NIR H−K/K space, we have shown only 3001 out of 33984 stars with photospheric emissions. In the first three panels, the extinction vectors are drawn using the average extinction laws from Flaherty et al. (2007). The positions of all the identified YSOs are shown in Figure 10a.

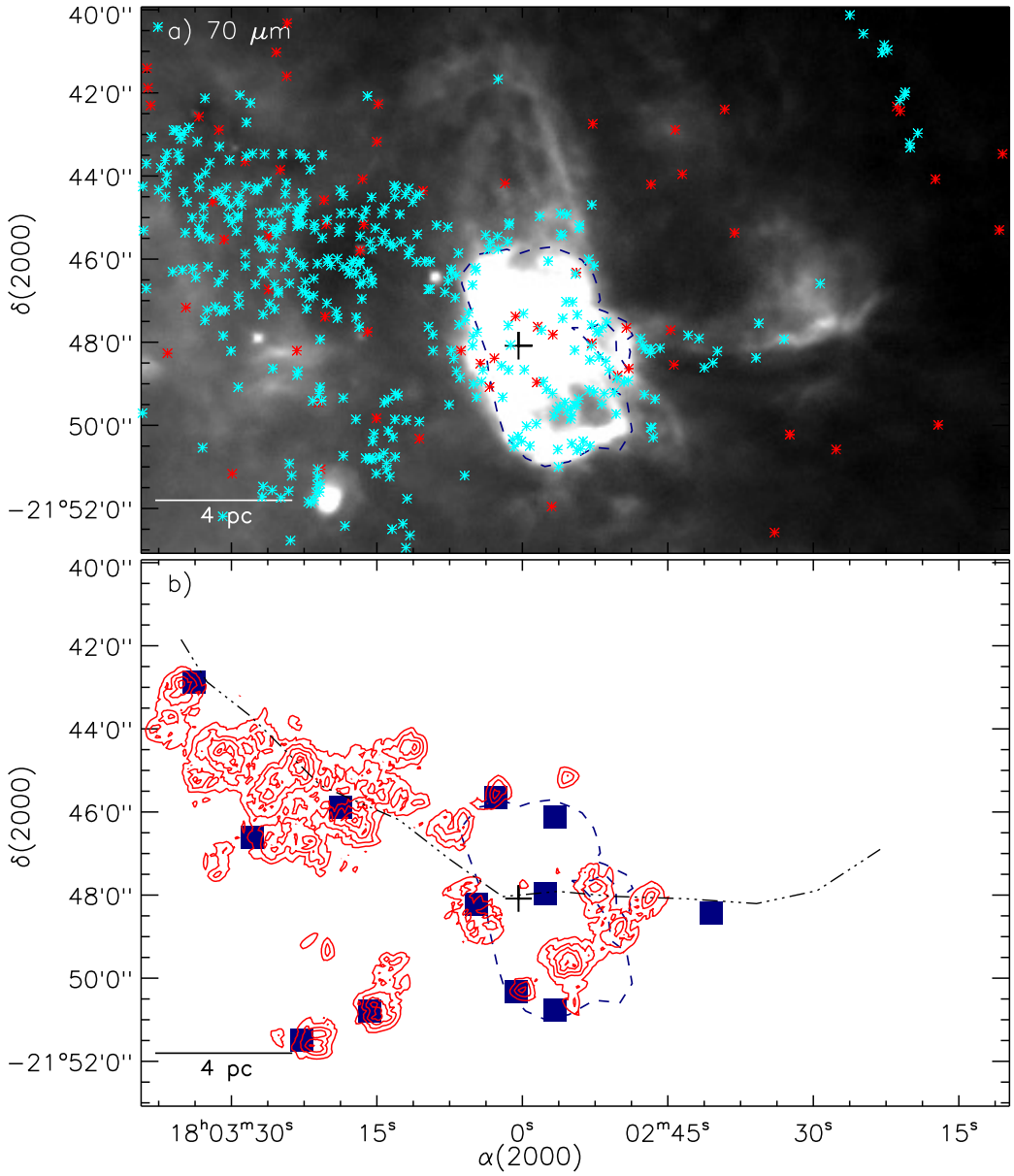

Figure 10. The spatial distribution of YSOs identified within the region probed in this paper using the NIR and MIR data. a) The asterisks represent the identified YSOs, which are overlaid on the 70 μm image. The YSOs selected using the GLIMPSE and MIPSGAL bands (see the first three panels in Figure 9) are shown by red color, whereas the cyan asterisks represent the YSOs identified using the NIR bands (see Figure 9d). b) Figure shows the surface density contours (in red) of all the identified YSOs. The contours are shown at 4, 6, 9, 15, and 25 YSOs/pc^2, from the outer to the inner side. The filled squares represent the positions of the identified *Herschel* clumps (see Table 1). A tight spatial association between YSOs clusters and clumps is evident. A bipolar nebula is also highlighted in both the panels similar to the one shown in Figure 4. An elongated filamentary structure is highlighted by a dashed-dotted curve. The position of IRAS 17599−2148 (+) is shown in both the panels. In both the panels, the scale bar at the bottom-left corner corresponds to 4 pc (at a distance of 4.2 kpc). Star formation activities are revealed toward the IRDC and bipolar nebula (see text for details).